



# Green synthesis, XRD/SAXS modelling and electrochemistry of indium iron oxide nanocomposite

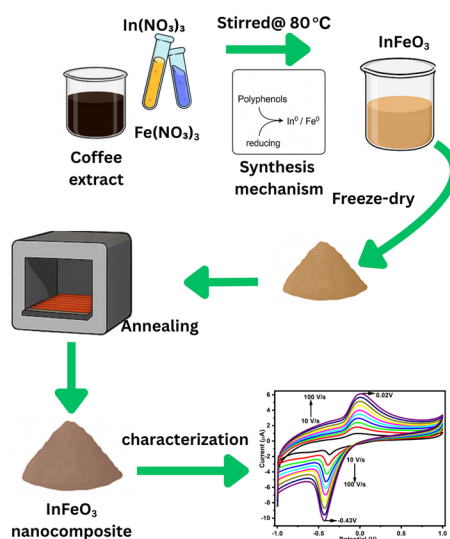
Nokwanda Precious Ngema<sup>1</sup> · Usisipho Feleni<sup>2</sup> · Ziyanda Tshobeni<sup>1</sup> · Jaymi January<sup>1</sup> · Takalani Mulaudzi<sup>3</sup> · Emmanuel Iwuoha<sup>1</sup> · Rachel Fanelwa Ngece-Ajayi<sup>1</sup>

Received: 19 March 2025 / Accepted: 26 June 2025 / Published online: 17 July 2025  
© The Author(s) 2025

## Abstract

A green synthesis approach was utilized to prepare indium iron oxide ( $\text{InFeO}_3$ ) nanocomposites using coffee extract as a reducing and capping agent. The structural, morphological, optical, and electrochemical properties of the synthesized materials were systematically characterized through X-ray diffraction (XRD), small-angle X-ray scattering (SAXS), high-resolution electron microscopy (HRTEM/HRSEM), Fourier-transform infrared spectroscopy (FTIR), UV–Vis spectroscopy, photoluminescence (PL), vibrating sample magnetometry (VSM), and Mössbauer spectroscopy. XRD analysis confirmed the formation of a rhombohedral  $\text{InFeO}_3$  structure with an average crystallite size of 27 nm, while HRTEM revealed spherical nanoparticles with partial agglomeration. SAXS and HRTEM data corroborated the nanoscale dimensions, with particle sizes ranging from 24 to 38 nm. Optical studies demonstrated a reduced bandgap (2.85 eV) for the composite compared to pure  $\text{In}_2\text{O}_3$  (3.3 eV) and  $\text{Fe}_2\text{O}_3$  (3.15 eV), attributed to charge transfer transitions between  $\text{Fe}^{3+}$  and  $\text{In}^{3+}$ . The nanocomposite exhibited enhanced magnetic properties, with a saturation magnetization ( $M_s$ ) of 18.48 emu/g, and Mössbauer spectroscopy revealed disrupted super-exchange interactions due to  $\text{In}^{3+}$  incorporation. Electrochemical analysis showed superior performance of the  $\text{InFeO}_3$ -modified electrode, characterized by a higher diffusion coefficient ( $9.72 \times 10^{-5} \text{ cm}^2 \text{ s}^{-1}$ ) and surface concentration ( $4.62 \times 10^{-7} \text{ mol cm}^{-2}$ ) compared to individual oxides, indicating improved charge transfer kinetics. These results highlight the potential of green-synthesized  $\text{InFeO}_3$  as a promising material for electrochemical sensing applications, combining sustainability with enhanced functional properties.

## Graphical abstract



**Keywords** Green synthesis · Indium iron oxide ( $\text{InFeO}_3$ ) · Nanocomposite · Coffee extract · Electrochemical sensor · Diffusion coefficient · Sustainable nanomaterials

## 1 Introduction

The escalating demand for advanced sensor and biosensor technologies is driving significant innovation in nanomaterials research. These materials, distinguished by their unique physicochemical properties at the nanoscale, offer a compelling pathway to miniaturization, cost-effective fabrication, and enhanced sensing performance, crucial for diverse applications spanning environmental monitoring to point-of-care diagnostics [1]. However, realizing the full potential of these technologies hinges on the development of novel nanocomposites with precisely tailored functionalities. A key challenge lies in refining the optical, electrochemical, and magnetic properties of these nanocomposites to achieve optimal sensor characteristics, including sensitivity and selectivity [2, 3]. Indium oxide ( $\text{In}_2\text{O}_3$ ), a prominent n-type semiconductor with a wide bandgap, is widely utilized in optical and electrical devices due to its inherent chemical reactivity and high carrier conductivity [4]. Iron oxide ( $\text{Fe}_2\text{O}_3$ ) nanoparticles present compelling advantages for biosensing applications, including biocompatibility, non-toxicity, thermal stability, and intriguing optical and magnetic behavior, alongside their natural abundance [5–7]. Despite these benefits, the synthesis of metal oxide-based sensors often requires high operating temperatures, limiting their practicality [8]. To address these challenges, green synthesis is an alternative, it offers a cost-effective and environmentally benign approach to nanomaterial fabrication, employing biological resources and mild reaction conditions to reduce environmental impact [9]. Green synthesis uses plant-based sources and involves the use of different parts of plants such as roots, leaves, flowers, fruits, and seeds [10–12]. These methods often utilize naturally derived reducing and capping agents, minimizing the use of hazardous chemicals and energy consumption [13]. In this study, we employed a green synthesis approach utilizing coffee extract as a reducing and capping agent for the synthesis of  $\text{InFeO}_3$  nanocomposites. Coffee is a readily available and cost-effective agricultural product and is rich in bioactive compounds such as polyphenols and organic acids [14]. These compounds can act as effective reducing agents for metal precursors and facilitate nanoparticle stabilization, offering a sustainable and eco-friendly alternative to traditional chemical synthesis methods [15]. The use of coffee extract in nanomaterial synthesis aligns with the principles of green chemistry, promoting sustainable and environmentally responsible nanotechnology. Incorporating metals and metal oxides with  $\text{In}_2\text{O}_3$  can

lead to sensors with improved sensitivity, selectivity, faster response, and recovery times, and crucially, reduced working temperatures [16, 17]. Notably,  $\text{Fe}_2\text{O}_3$  nanoparticles offer distinct advantages in electrochemical sensing due to their intrinsic electrical conductivity at room temperature, arising from rapid electron exchange between  $\text{Fe}^{2+}$  and  $\text{Fe}^{3+}$  ions [18]. Recent investigations have focused on transition element (TE) doped indium oxide magnetic semiconductors, with iron (Fe) doped  $\text{In}_2\text{O}_3$  attracting significant attention. This interest stems from Fe-doped  $\text{In}_2\text{O}_3$ 's excellent electrical conductivity, high transparency in the visible spectrum, and the favorable incorporation of Fe into the  $\text{In}_2\text{O}_3$  lattice [19, 20]. While research has explored the magnetic properties of Fe-doped  $\text{In}_2\text{O}_3$ , revealing phenomena such as room temperature ferromagnetism and paramagnetism [21, 22]. Our study addresses the critical gap in the literature by focusing on the green synthesis of  $\text{InFeO}_3$  nanocomposite using coffee extract and conducting a comprehensive investigation of their structural, morphological, optical, and electrochemical properties. To the best of our knowledge, this work represents the first detailed electrochemical characterization of a green synthesized  $\text{InFeO}_3$  nanocomposite material, specifically evaluated as a modifier for glassy carbon electrodes.

## 2 Experimental procedure

### 2.1 Reagents and sample preparation

Indium (III) nitrate hydrate (99.9%), iron nitrate nonahydrate (99.99%), sodium dihydrogen phosphate monobasic anhydrous ( $\text{H}_2\text{NaPO}_4$ ) (>99%), disodium hydrogen phosphate dibasic ( $\text{HNa}_2\text{PO}_4$ ) (>98%), were purchased from Sigma Aldrich, South Africa. Kilimanjaro ground coffee was purchased from a local Woolworths shop. Lamivudine and abacavir drug were also purchased from Sigma Aldrich, South Africa. The alumina micro polishing pads and polishing powder (0.05, 0.3 and 1.0 micron) were obtained from Buehler, 26 LL, USA. 0.1 M phosphate buffer solution, pH 7.4 was prepared from disodium hydrogen phosphate dibasic and sodium dihydrogen phosphate monobasic using Milli Q water purification. Lamivudine and abacavir drugs were used without any purification and dissolved in 0.1 M PBS pH 7.4, urine and plasma and the undissolved components were removed using filtering through a Whatman polytetrafluoroethylene syringe filter (pore size 0.3  $\mu\text{m}$ ). 0.1 M phosphate

buffer solution (PBS) with pH 7.4 was prepared from sodium phosphate monobasic dihydrate ( $\text{H}_2\text{NaO}_4\text{P}_2\text{H}_2\text{O}$ ) and sodium phosphate dibasic dehydrate ( $\text{HNa}_2\text{O}_4\text{P}_2\text{H}_2\text{O}$ ); was used as the electrolytic solution throughout the course of this study unless stated otherwise. The PBS solution was kept refrigerated at 4 °C when not in use.

## 2.2 Preparation of the coffee extract

An aqueous coffee extract was prepared to serve as a green reducing and capping agent. 8 g of ground coffee was added to 400 mL of deionized water. The mixture was heated to 80 °C and stirred for 1 h. After cooling, the solution was filtered through Whatman filter paper (0.3  $\mu\text{m}$ ) to remove solid residues. The resulting brown coffee extract solution was stored at 4 °C.

## 2.3 Green synthesis of $\text{In}_2\text{O}_3$ , $\text{Fe}_2\text{O}_3$ , and $\text{InFeO}_3$ nanomaterials

All nanomaterials were synthesized using a common procedure involving reduction in coffee extract followed by freeze-drying and annealing.

- Synthesis of  $\text{In}_2\text{O}_3$ : 8 g of indium (III) nitrate hydrate ( $\text{In}(\text{NO}_3)_3 \cdot x\text{H}_2\text{O}$ ) was dissolved into the prepared coffee extract. The mixture was heated at 80 °C for 2 h with constant stirring.
- Synthesis of  $\text{Fe}_2\text{O}_3$ : Iron (III) nitrate nonahydrate ( $\text{Fe}(\text{NO}_3)_3 \cdot 9\text{H}_2\text{O}$ ) and the coffee extract were mixed in a 1:2 volume ratio, then heated at 80 °C for 2 h with constant stirring.
- Synthesis of  $\text{InFeO}_3$  Nanocomposite: The composite was prepared by dissolving equimolar amounts of  $\text{In}(\text{NO}_3)_3 \cdot x\text{H}_2\text{O}$  and  $\text{Fe}(\text{NO}_3)_3 \cdot 9\text{H}_2\text{O}$  into the coffee extract. The mixture was then heated at 80 °C for 2 h with constant stirring.

For all preparations, the resulting solutions were freeze-dried for 48 h to obtain a precursor powder. This powder was then annealed in a furnace at 800 °C for 2 h. The 800 °C annealing temperature was chosen based on the analysis of coffee extract-derived precursors shows complete organic residue decomposition occurs between 750 and 800 °C, ensuring pure oxide formation without carbon contamination. The final products for all three materials were further characterized using different techniques. The core reaction mechanism involving the reduction of  $\text{In}^{3+}$  and  $\text{Fe}^{3+}$  ions by polyphenolic compounds in the coffee extract, which act as both reducing and capping agent, is shown in the schematic Fig. 1.

## 2.4 Electrode preparation and modification

Before the electrochemistry analysis on the bare GCE and modified GCE with  $\text{In}_2\text{O}_3$ ,  $\text{Fe}_2\text{O}_3$  and  $\text{InFeO}_3$ , the working electrode (i.e., GCE) was polished using alumina slurries. The electrochemical features of the bare and modified electrodes were investigated using cyclic voltammograms at 50  $\text{mVs}^{-1}$  in 0.1 M PBS, pH 7.4. Diffusion co-efficient and surface charge were calculated using Eqs. (4) and (5).

## 2.5 Characterization techniques

XRD in this study was used to study the structural properties, orientation of a single grain, phase structure and composition, crystallite size, and lattice parameters of the synthesized nanomaterials. Measurements were performed using a multipurpose X-ray diffractometer D8-Advance from Bruker operated in a continuous  $\alpha$ - $\alpha$  scan in locked-coupled mode with  $\text{Cu-K}\alpha$  radiation. Ultraviolet–visible (UV–Vis) spectroscopy was carried out on a Nicolet Evolution 100 from Thermo Electron Corporation, Altrincham, UK. The nanoparticles were dispersed in distilled water solution within a wavelength range of 200–600 nm, the distilled water was also used as a baseline. PL measurements for this study were obtained using NanoLog from Horiba Jobin Yvon, Edison, NJ, USA. FTIR measurements for this study were performed using FTIR spectrometer Spectrum Two (PerkinElmer, Waltham, USA) in a spectral range of 500–4000  $\text{cm}^{-1}$ . The solid sample was mixed with potassium bromide (KBr) to make a pellet suitable for FTIR measurements using hand press manual KBr tool. The FTIR background correction was made using a reference blank potassium bromide pellet. HRTEM images were taken using Tecnai G2 F20X-Twin MAT 200 kV Field Emission Transmission Microscopy from FEI (Eindhoven, The Netherlands). The analysis for this study was done using Tescan MIRA3 RISE SEM from Tescan, Brno, Czech Republic and elemental analysis was done using FEI NovaNano SEM from FEI company, hillsboro, OR, USA.

## 3 Results and discussion

### 3.1 XRD analysis

The structural and phase characteristics of the synthesized  $\text{In}_2\text{O}_3$ ,  $\text{Fe}_2\text{O}_3$ , and  $\text{InFeO}_3$  materials were thoroughly investigated using X-ray Diffraction (XRD). Figure 2a presents the XRD patterns, confirming the crystalline nature and phase purity of the synthesized materials. For  $\text{In}_2\text{O}_3$ , the diffraction pattern exhibits characteristic peaks corresponding to the (222), (400), (440), and (622) planes, among others, which are in excellent agreement with the standard reference data

**Fig. 1** Schematic synthesis procedure for the  $\text{InFeO}_3$  nanocomposite

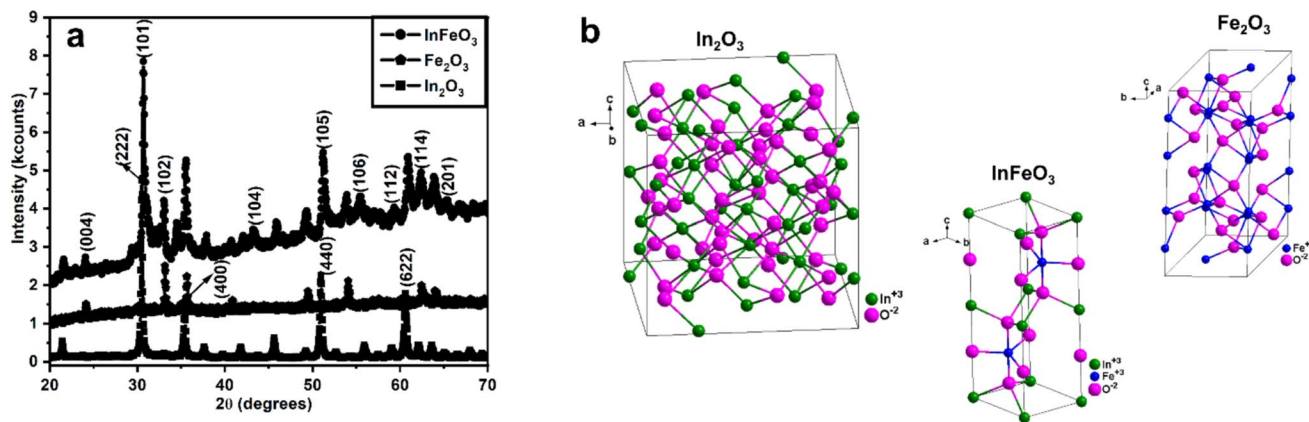
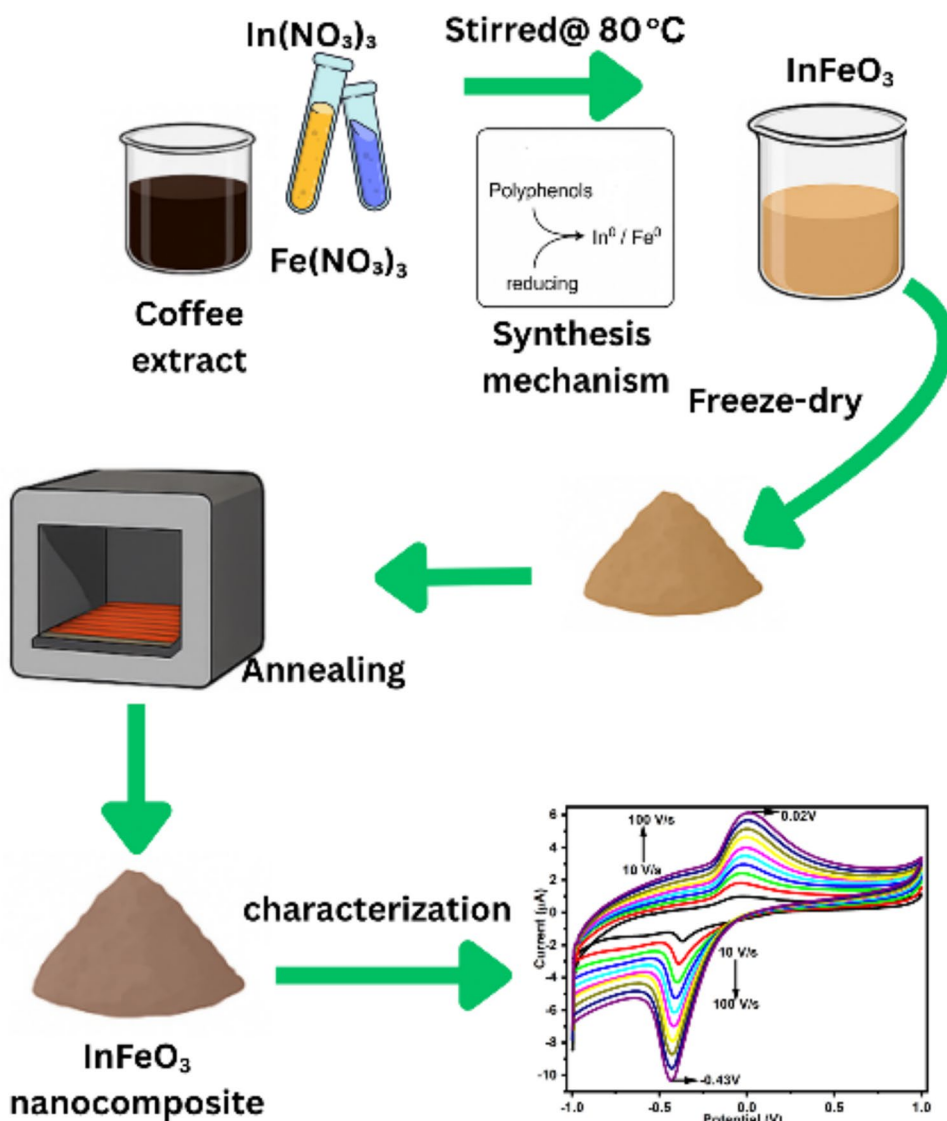


**Fig. 2** **a** XRD patterns and crystal structures of  $\text{In}_2\text{O}_3$ ,  $\text{Fe}_2\text{O}_3$ , and  $\text{InFeO}_3$ , and **b** crystal structures annealed at  $800\text{ }^\circ\text{C}$

for cubic  $\text{In}_2\text{O}_3$  (JCPDS No. 06–0416) [23], thus confirming the formation of single-phase, crystalline indium oxide with a cubic structure. Similarly, the XRD pattern of  $\text{Fe}_2\text{O}_3$  displays diffraction peaks at  $2\theta$  positions consistent with the (012), (104), (110), (024), (116), (214), and (300) planes, unequivocally indexed to the rhombohedral hematite structure of  $\text{Fe}_2\text{O}_3$ , as corroborated by JCPDS No. 33-0664, in line the study by Prerna et al. [24]. The absence of any additional diffraction peaks in both  $\text{In}_2\text{O}_3$  and  $\text{Fe}_2\text{O}_3$  patterns indicates the high phase purity and lack of detectable impurities in the individual oxide materials. The XRD pattern of the  $\text{InFeO}_3$  nanocomposite in Fig. 2a exhibits a superposition of diffraction peaks from both  $\text{In}_2\text{O}_3$  and  $\text{Fe}_2\text{O}_3$  phases, suggesting the successful formation of a biphasic composite material. The  $\text{InFeO}_3$  diffraction pattern was matched against JCPDS No. 41–0038 standard data, further supporting the coexistence of both constituent phases within the composite. While a visual inspection suggests an equal contribution of  $\text{In}_2\text{O}_3$  and  $\text{Fe}_2\text{O}_3$  phases, the (101) reflection in the  $\text{InFeO}_3$  pattern shows a significantly enhanced relative intensity, indicating a preferential crystallographic orientation, possibly suggesting anisotropic growth of the  $\text{In}_2\text{O}_3$  phase within the composite. This preferential orientation could be related to the synthesis conditions or the interfacial interactions between the  $\text{In}_2\text{O}_3$  and  $\text{Fe}_2\text{O}_3$  phases. Furthermore, a subtle but noteworthy shift in the peak positions of  $\text{InFeO}_3$  toward higher  $2\theta$  values is observed in comparison to the peaks of pure  $\text{In}_2\text{O}_3$ . This peak shift is indicative of a lattice contraction within the  $\text{In}_2\text{O}_3$  phase in the composite. This contraction is likely induced by the partial substitution of larger  $\text{In}^{3+}$  ions (0.800 Å) by smaller  $\text{Fe}^{3+}$  ions (0.645 Å) at octahedral sites. Consistent with the findings of previous studies on similar  $\text{InFeO}_3$  composites where ionic substitution led to lattice distortions [25, 26], our observation supports the hypothesis of  $\text{Fe}^{3+}$  ions partially incorporating into the  $\text{In}^{3+}$  lattice. To estimate the average crystallite size ( $D$ ), the Debye–Scherrer equation [27] was used:

$$D = K\lambda/(\beta\cos\theta) \quad (1)$$

where  $K$  is the Scherrer constant (0.89),  $\lambda$  is the X-ray wavelength,  $\theta$  is the Bragg angle, and  $\beta$  is the Full Width at Half Maximum (FWHM) of the diffraction peak in radians. Using the FWHM of the (222) peak for  $\text{In}_2\text{O}_3$ , (104) peak for  $\text{Fe}_2\text{O}_3$ , and (101) peak for  $\text{InFeO}_3$ , the average crystallite sizes were estimated to be approximately 34 nm, 38 nm, and 28 nm, respectively. These values suggest a reduction in crystallite size in the  $\text{InFeO}_3$  composite compared to the individual oxides, which could contribute to the enhanced peak intensity observed in the composite. Figure 2b illustrates the crystal structures of  $\text{In}_2\text{O}_3$ ,  $\text{Fe}_2\text{O}_3$ , and  $\text{InFeO}_3$  nanoparticles.  $\text{In}_2\text{O}_3$  is depicted with a cubic structure, a complex arrangement within its unit cell characterized by

two non-equivalent indium positions within oxygen octahedral and trigonal prismatic coordination [28].  $\text{Fe}_2\text{O}_3$  is shown with a rhombohedral structure of the corundum type, where  $\text{Fe}^{3+}$  ions occupy two-thirds of the octahedral sites in a close-packed oxygen lattice [29]. The  $\text{InFeO}_3$  composite is represented with a hexagonal crystal structure, featuring both octahedral and trigonal bipyramidal coordination environments. In this structure, Indium atoms are in octahedral interstices of oxygen layers, while Fe atoms are coordinated in a trigonal bipyramidal manner within hexagonal layers [30]. The differences in crystallite size observed in the composite could be related to the distinct coordination structures and growth mechanisms of  $\text{In}_2\text{O}_3$  and  $\text{Fe}_2\text{O}_3$ .

### 3.2 HRTEM of the composite material

The morphological characteristics and particle size distributions of the synthesized  $\text{In}_2\text{O}_3$ ,  $\text{Fe}_2\text{O}_3$ , and  $\text{InFeO}_3$  nanoparticles were investigated using High-Resolution Transmission Electron Microscopy (HRTEM). Figure 3a, d, g displays representative HRTEM micrographs of  $\text{In}_2\text{O}_3$ ,  $\text{Fe}_2\text{O}_3$ , and  $\text{InFeO}_3$  nanoparticles, respectively acquired at a 50 nm magnification scale. The HRTEM micrograph of  $\text{In}_2\text{O}_3$  NPs (Fig. 3a) reveals a morphology characterized by well-dispersed, predominantly spherical particles with an average particle size of 31.9 nm. The image also suggests some degree of particle interaction, evidenced by darker areas potentially indicating regions of proximity or aggregation of smaller particles leading to the formation of larger entities. Figure 3d for  $\text{Fe}_2\text{O}_3$  nanoparticles appear less uniformly spherical and exhibit a more irregular, somewhat plate-like or faceted shape. While some degree of aggregation is also visible, the overall particle morphology is more angular and less smoothly rounded than the  $\text{In}_2\text{O}_3$  particles. In the case of  $\text{InFeO}_3$  (Fig. 3g), the nanoparticles also exhibit a generally spherical morphology, although with a noticeable degree of agglomeration. This agglomeration may be attributed to the high annealing temperature of 800 °C used during synthesis, which promoted particle sintering and reduced surface energy by forming larger aggregates [31]. While this agglomeration might be considered a drawback in some applications, it could also be advantageous in others, such as sensor applications, where enhanced magnetic interactions between nanoparticles within aggregates may lead to improved device performance, as suggested in previous studies [32, 33]. Selected Area Electron Diffraction (SAED) patterns were acquired for each sample to assess their crystallinity, as shown in Fig. 3b, e, h for  $\text{In}_2\text{O}_3$ ,  $\text{Fe}_2\text{O}_3$ , and  $\text{InFeO}_3$ , respectively. The SAED pattern for  $\text{In}_2\text{O}_3$  (Fig. 3b) exhibits continuous diffraction rings, characteristic of a polycrystalline material. The rings are indexed to specific crystallographic planes of cubic  $\text{In}_2\text{O}_3$ , consistent with the XRD findings. Similarly, the SAED patterns for  $\text{Fe}_2\text{O}_3$  (Fig. 3e) and

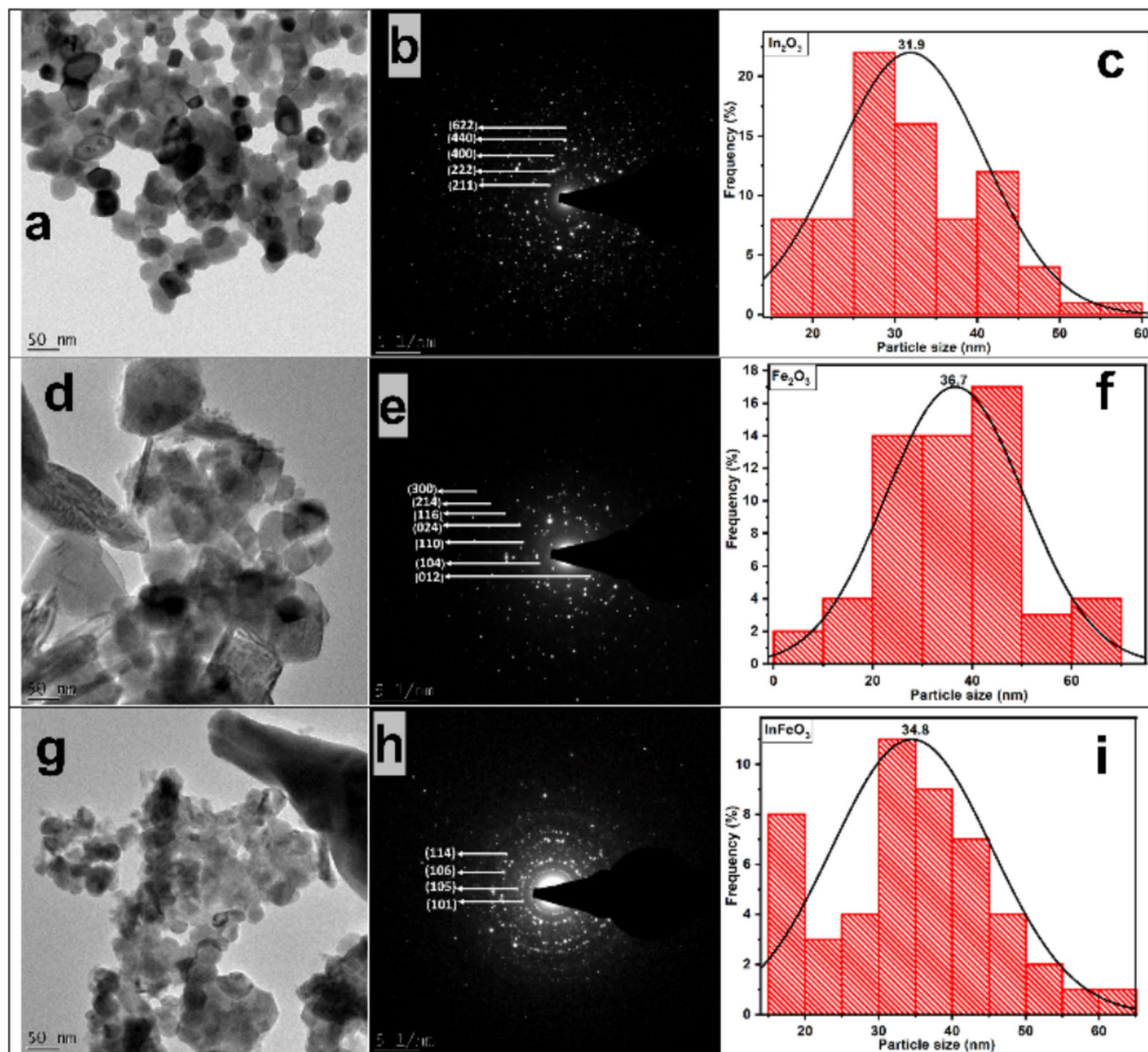


**Fig. 3** HRTEM images, SAED and particle size distribution histogram of  $\text{In}_2\text{O}_3$  (a–c),  $\text{Fe}_2\text{O}_3$  (d and e) and  $\text{InFeO}_3$  (h and i)

$\text{InFeO}_3$  (Fig. 3h) also display ring patterns, further confirming their polycrystalline nature, which aligns well with the polycrystalline structures inferred from XRD analysis. However, in the SAED patterns of  $\text{Fe}_2\text{O}_3$  and  $\text{InFeO}_3$ , the presence of superimposed bright diffraction spots alongside the rings suggests the existence of larger, more ordered crystallites or regions of preferred orientation within the polycrystalline matrix [34, 35]. This observation indicates a degree of textural heterogeneity in these materials, which could influence their macroscopic properties. Particle size distribution histograms, derived from TEM image analysis, are presented in Fig. 3c, f, i for  $\text{In}_2\text{O}_3$ ,  $\text{Fe}_2\text{O}_3$ , and  $\text{InFeO}_3$  respectively. The

histograms, fitted with Gaussian distributions, reveal average particle sizes of 31.9 nm for  $\text{In}_2\text{O}_3$ , 36.7 nm for  $\text{Fe}_2\text{O}_3$ , and 34.8 nm for  $\text{InFeO}_3$ . These TEM-derived particle sizes are in reasonable agreement with the crystallite sizes estimated from XRD using the Debye–Scherrer equation (reported as approximately 34 nm, 38 nm, and 28 nm for  $\text{In}_2\text{O}_3$ ,  $\text{Fe}_2\text{O}_3$ , and  $\text{InFeO}_3$ , respectively). The slight discrepancies between TEM particle size and XRD crystallite size measurements could arise from several factors. XRD measures the size of coherently diffracting domains (crystallite size), which may be smaller than the actual particle size observed in HRTEM, especially if the particles are polycrystalline aggregates of

smaller crystallites. Furthermore, HRTEM provides a direct measurement of particle dimensions, while XRD-derived crystallite size is an average estimate based on peak broadening. The overall agreement between the two techniques, however, validates the nanoscale dimensions of the synthesized materials.

### 3.3 Morphological properties of the composite material

The surface morphology and elemental composition of the synthesized  $\text{In}_2\text{O}_3$ ,  $\text{Fe}_2\text{O}_3$ , and  $\text{InFeO}_3$  materials were further characterized using High-Resolution Scanning

Electron Microscopy (HRSEM) coupled with Energy Dispersive X-ray Spectroscopy (EDS). Figure 4a, c and e presents HRSEM micrographs and corresponding EDS spectra with elemental composition insets (b, d, f) for  $\text{In}_2\text{O}_3$ ,  $\text{Fe}_2\text{O}_3$ , and  $\text{InFeO}_3$  respectively. The HRSEM micrograph of  $\text{In}_2\text{O}_3$  nanoparticles (Fig. 4a) reveals a morphology characterized by near-spherical particles with a relatively uniform size distribution. These particles appear to be moderately aggregated, forming clusters but still maintaining discernible individual particle boundaries. To assess the elemental purity and stoichiometry, EDS analysis was performed. The EDS spectrum Fig. 4b and the inset table demonstrate the presence of indium (In) and oxygen (O) as the primary

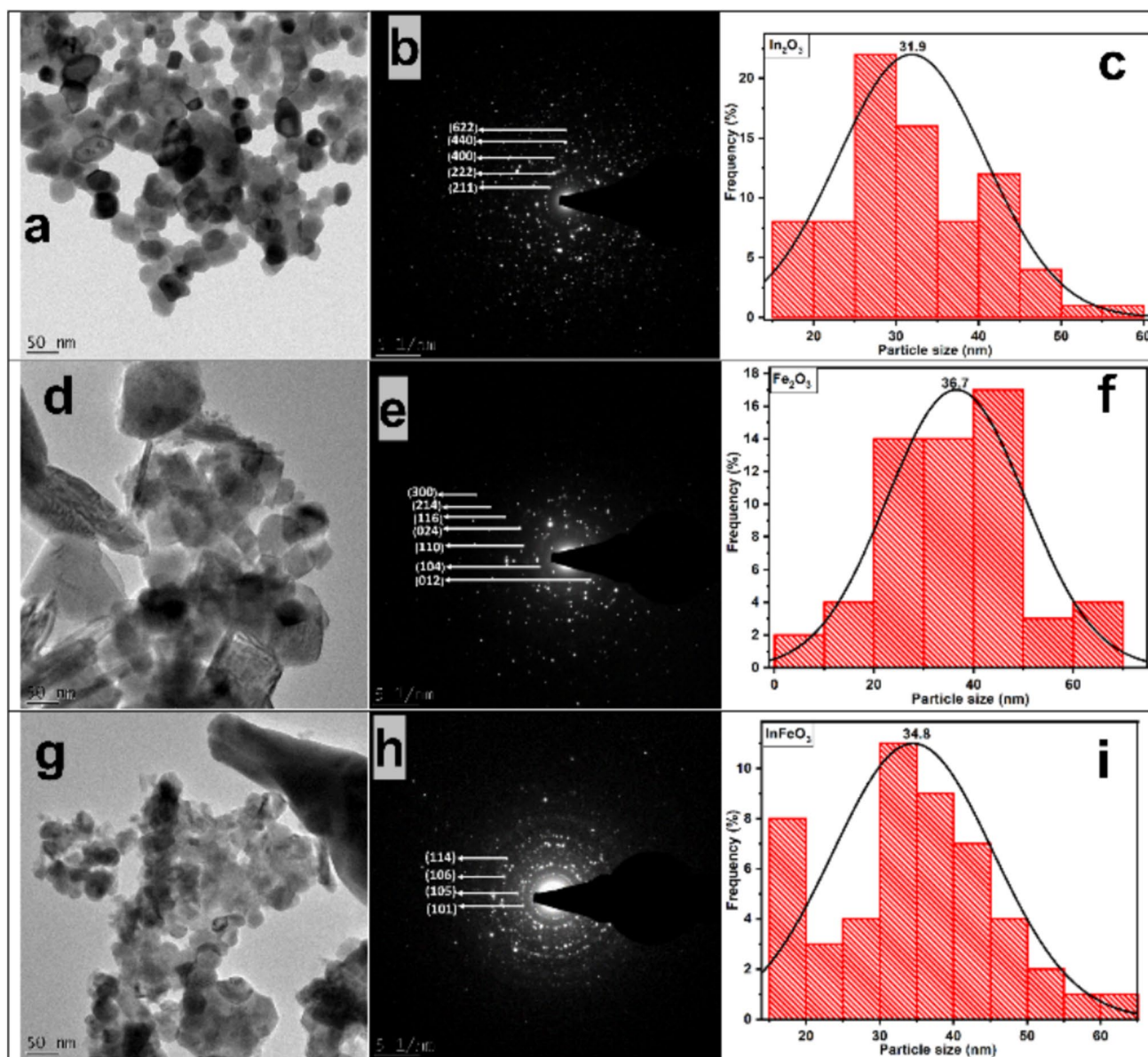


**Fig. 4** HRSEM, EDS and elemental composition (inset) of  $\text{In}_2\text{O}_3$  (a and b),  $\text{Fe}_2\text{O}_3$  (c and d), and  $\text{InFeO}_3$  (e and f) NPs annealed at 800 °C

elemental constituents. Quantitative analysis from EDS indicates a weight percentage of 80.48% for indium and 19.52% for oxygen. This elemental ratio is in close agreement with the stoichiometric proportions expected for  $\text{In}_2\text{O}_3$ , confirming the high purity and chemical identity of the synthesized indium oxide nanoparticles. The HRSEM image of  $\text{Fe}_2\text{O}_3$  nanoparticles (Fig. 4c) shows a distinct morphology compared to  $\text{In}_2\text{O}_3$ .  $\text{Fe}_2\text{O}_3$  particles appear to have a more irregular, clustered shape, with less defined individual particle boundaries and a more interconnected network-like structure. EDS analysis (Fig. 4d) of the  $\text{Fe}_2\text{O}_3$  sample confirms that iron (Fe) and oxygen (O) are the dominant elements. The inset table provides a weight percentage of 81.5% Fe and 18.5% O, which is consistent with the expected elemental composition of  $\text{Fe}_2\text{O}_3$ , indicating the successful synthesis of high-purity iron oxide nanoparticles. The HRSEM micrograph of the  $\text{InFeO}_3$  composite material (Fig. 4e) displays agglomerated particles that appear to be nearly spherical but form larger, irregular clusters with noticeable voids and inter-particle spaces within the agglomerates. The observed agglomeration in  $\text{InFeO}_3$ , similar to that seen in  $\text{Fe}_2\text{O}_3$ , could be attributed to factors such as a relatively small volume of stabilizing agent used during synthesis, leading to a high surface area to volume ratio and consequently stronger inter-particle attractive forces [32]. EDS analysis of the  $\text{InFeO}_3$  sample (Fig. 4f) confirms the presence of indium (In), iron (Fe), and oxygen (O) as the major elemental components. The inset table quantifies the elemental weight percentages as approximately 41.26% for indium, 31.6% for iron, and 22.52% for oxygen. The presence of both indium and iron in significant proportions confirms the successful co-incorporation of these elements into the synthesized  $\text{InFeO}_3$  composite. A minor carbon (C) signal is also detected in the EDS spectrum of  $\text{InFeO}_3$ ,

which could be attributed to residual carbon from the synthesis process or from the carbon coating typically used for SEM sample preparation to enhance conductivity and reduce charging effects.

### 3.4 Internal structure of the composite material

Small-Angle X-ray Scattering (SAXS) was used to investigate the particle size, shape, and internal structure of the synthesized nanoparticles in the size range of 1–100 nm. This technique, utilizing a model-free approach, allows for the determination of geometric parameters directly from the scattering intensity curve, providing insights into particle volume, molecular mass, forward scattering, radius of gyration, surface area per unit volume, largest dimension, and the pair distance distribution function (PDDF) [36, 37]. The scattering process is characterized by the scattering vector,  $q$ , defined by Eq. 2:

$$q = (4\pi \sin(\theta)) / \lambda \quad (2)$$

where  $\lambda$  is the wavelength of the incident X-ray radiation ( $\text{Cu-K}\alpha$ ,  $\lambda = 0.15406$  nm), and  $\theta$  is half the scattering angle. To validate the internal structures of the nanoparticles, model-free PDDF profiles and size distributions by intensity were analyzed, as presented in Fig. 5a and b. Figure 5a illustrates the PDDF curves for  $\text{In}_2\text{O}_3$ ,  $\text{Fe}_2\text{O}_3$ , and  $\text{InFeO}_3$ . The PDDF curves for all three materials exhibit asymmetrical, bell-shaped characteristics, indicative of predominantly spherically shaped nanoparticles. The maximum radii ( $r$ ) derived from the PDDF curves, representing the longest dimension within the majority of the nanoparticles, are approximately 26 nm for  $\text{In}_2\text{O}_3$ , 27.8 nm for  $\text{Fe}_2\text{O}_3$ , and 25.2 nm for  $\text{InFeO}_3$ . Furthermore, the PDDF curves also

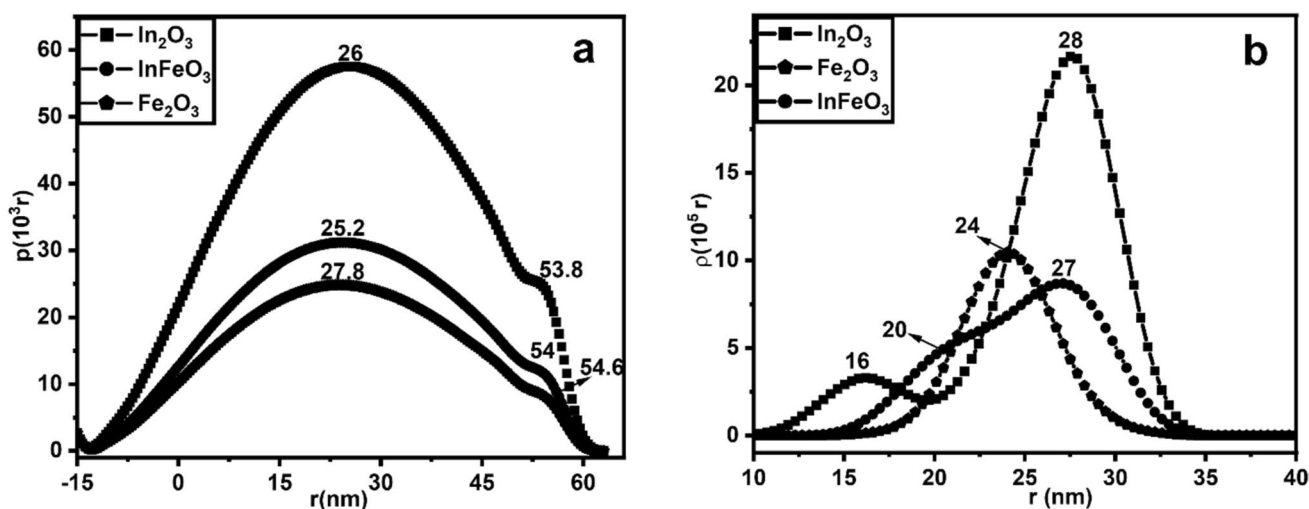


Fig. 5 Pair distance distribution functions (a) and size distribution by intensity (b) of  $\text{In}_2\text{O}_3$ ,  $\text{Fe}_2\text{O}_3$ , and  $\text{InFeO}_3$  annealed at 800 °C

display minor shoulders or extended tails at larger radii values, specifically around 53 nm for  $\text{In}_2\text{O}_3$ , 54.6 nm for  $\text{Fe}_2\text{O}_3$ , and 54 nm for  $\text{InFeO}_3$ . These features suggest the presence of some larger agglomerated particles within each sample, consistent with the agglomeration observed in HRTEM and HRSEM images. Figure 5b presents the size distributions by intensity for  $\text{In}_2\text{O}_3$ ,  $\text{Fe}_2\text{O}_3$ , and  $\text{InFeO}_3$ . These distributions reveal that the nanoparticles are polydisperse, exhibiting a range of particle sizes. The peak positions in the size distribution by intensity, which are weighted towards larger particles due to the scattering intensity being proportional to the sixth power of the particle size [38], indicate average radii of approximately 28 nm for  $\text{In}_2\text{O}_3$ , 24 nm for  $\text{Fe}_2\text{O}_3$ , and 27 nm for  $\text{InFeO}_3$ . Additionally, smaller secondary peaks are observed in the size distributions, notably at around 16 nm and 20 nm, suggesting the presence of a sub-population of smaller particles, particularly evident in the  $\text{In}_2\text{O}_3$  and  $\text{Fe}_2\text{O}_3$  nanoparticles. Compared to other techniques (XRD and HRTEM), the average radii derived from SAXS (25–28 nm based on peak positions in size distribution by intensity) are generally smaller than the average particle sizes estimated from HRTEM (31.9 nm for  $\text{In}_2\text{O}_3$ , 36.7 nm for  $\text{Fe}_2\text{O}_3$ , and 34.8 nm for  $\text{InFeO}_3$ ). However, the maximum radii from PDDF (25–28 nm) are in closer agreement with the XRD crystallite sizes 34 nm, 38 nm, and 28 nm for  $\text{In}_2\text{O}_3$ ,  $\text{Fe}_2\text{O}_3$ , and  $\text{InFeO}_3$ , respectively, as shown in Table 1. These apparent differences can be attributed to several factors. SAXS is sensitive to the overall size and shape of the particles in solution or powder form, and the size distribution by intensity is weighted towards larger particles. HRTEM, on the other hand, directly visualizes individual particles and their aggregates, potentially capturing a broader range of particle sizes and agglomerates, leading to slightly larger average particle sizes. XRD, using the Debye–Scherrer equation, estimates the *crystallite* size, which represents the coherently diffracting domain within a particle. If particles are polycrystalline (as indicated by SAED), the crystallite size from XRD would be expected to be smaller than the overall particle size observed in TEM. However, in this case, the XRD crystallite sizes are somewhat comparable to or even slightly larger than the SAXS radii. SAXS radii are somewhat smaller than HRTEM particle sizes and could be related to the core–shell structure of nanoparticles or to the presence of a surface layer with different scattering properties, which SAXS might

**Table 1** Summary and comparison of particle size obtained from XRD, HRTEM and SAXS

Material	XRD (nm)	HRTEM (nm)	SAXSpace (nm)
$\text{In}_2\text{O}_3$	34	31.9	27.6
$\text{Fe}_2\text{O}_3$	38	36.7	24
$\text{InFeO}_3$	27.3	34.8	27

not fully capture in the same way as the TEM imaging [39]. Additionally, the polydispersity of the samples, as evidenced by both SAXS size distributions and HRTEM images, complicates direct size comparisons between different techniques, as each method is sensitive to different aspects of the size distribution. Despite these differences, the SAXS, HRTEM, and XRD data collectively confirm that the synthesized materials consist of nanoparticles in the nanoscale regime, with average dimensions in the range of 25–38 nm, and exhibit a degree of polydispersity and agglomeration.

### 3.5 Structural features of the composite material

The FTIR spectra showing several significant absorption peaks is shown in Fig. 6. FTIR was used to validate the major functional groups that were involved in the synthesis and stabilization of the synthesized NPs. The absorption around 3000–3400  $\text{cm}^{-1}$  observed for all three NPs, are attributed to the OH stretching vibrations of polyphenolic groups from the coffee extract. The absorption bands observed below 1000  $\text{cm}^{-1}$  wavenumber in are responsible for the inter atomic vibrations and this region is called the fingerprint region of the FTIR spectra [40]. 1018  $\text{cm}^{-1}$  for the  $\text{InFeO}_3$  can be attributed to In-Fe broadening. The absorption peak around 607, 565 and 429  $\text{cm}^{-1}$  are characteristic of cubic  $\text{In}_2\text{O}_3$ , to the lattice vibration of In-O in  $\text{In}_2\text{O}_3$  [41, 42]. Bands around 1380 & 1630  $\text{cm}^{-1}$  can be attributed to the nitrate group and bend deformation of water molecules. The band peak observed at 1562  $\text{cm}^{-1}$  was assigned as the C-O stretching vibration mode the appearance of CO band was due to the association of the extract unit with indium ions ( $\text{In}^{3+}$ ) to produce a longer chain and facilitate self-assembly to become an orderly

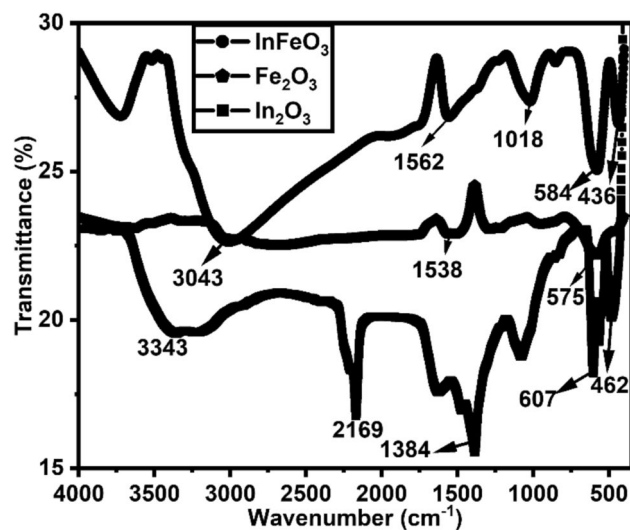


**Fig. 6** FTIR spectra of  $\text{In}_2\text{O}_3$ ,  $\text{Fe}_2\text{O}_3$  and  $\text{InFeO}_3$  annealed at 800 °C

shape through van der Waals interactions [43]. The band around  $2375\text{ cm}^{-1}$  is due to the absorption of  $\text{CO}_2$ , which may be due to the moisture absorption from the atmosphere after annealing [41].  $\text{Fe}_2\text{O}_3$  exhibited an absorption band around  $578\text{ cm}^{-1}$  which is attributed the deformation of Fe–O in the octahedral and tetrahedral region of a hematite [44, 45]. Bands located at  $1570\text{--}1520\text{ cm}^{-1}$ ; assigned to coupling between N–H bend and C–N stretch [46]. The  $\text{InFeO}_3$  had peaks like  $\text{In}_2\text{O}_3$ , and  $\text{Fe}_2\text{O}_3$ , around  $584$  and  $436\text{ cm}^{-1}$ . However, the slight shift and the sharpness in the peak at  $584\text{ cm}^{-1}$  confirmed the changes in the bonding environments [47].

### 3.6 Optical properties of the composite

UV–visible absorption spectroscopy was widely used to examine the optical properties of the NPs. Figure 7a shows absorption bands of  $\text{InFeO}_3$ ,  $\text{In}_2\text{O}_3$ , and  $\text{Fe}_2\text{O}_3$  NPs which are found to be around  $322\text{ nm}$ ,  $340\text{ nm}$ , and  $320\text{ nm}$ ,

respectively. The bands were generated from transition of electrons from the valence band to the conduction band, these values are consistent with some existing literature [48, 49]. The absorption band at  $320\text{ nm}$  results from the ligand to metal charge transfer transitions from the  $\text{Fe}^{3+}$  d-d ligand field transitions. Similar results were reported for the preparation of  $\alpha\text{-Fe}_2\text{O}_3$  nanoparticles by oxygenating pure iron, where the absorption band was found at  $310\text{ nm}$  and was assigned to the  ${}^6\text{A}_1\text{-}{}^4\text{T}_1$  ( ${}^4\text{P}$ ) [50, 51]. As observed in Fig. 7a, the absorption wavelength of the  $\text{InFeO}_3$  composite relayed more to the wavelength of  $\text{Fe}_2\text{O}_3$ , the absorption band obtained for  $\text{Fe}_2\text{O}_3$  NPs at  $320\text{ nm}$  red-shifted to  $322\text{ nm}$  by the  $\text{InFeO}_3$ , which could have resulted from coupling the  $\text{Fe}_2\text{O}_3$  with  $\text{In}_2\text{O}_3$  NPs. This may be due to the d-orbitals overlapping, that is consisting of the  $5s$  or  $\text{Fe } 3d$  orbitals. The difference in the band gap of  $\alpha\text{-Fe}_2\text{O}_3$  and  $\text{In}_2\text{O}_3$  will cause the realignment of the conduction band (CB) and valence band (VB) in the energy band structure of  $\text{InFeO}_3$  resulting in the red-shift observed for the absorption

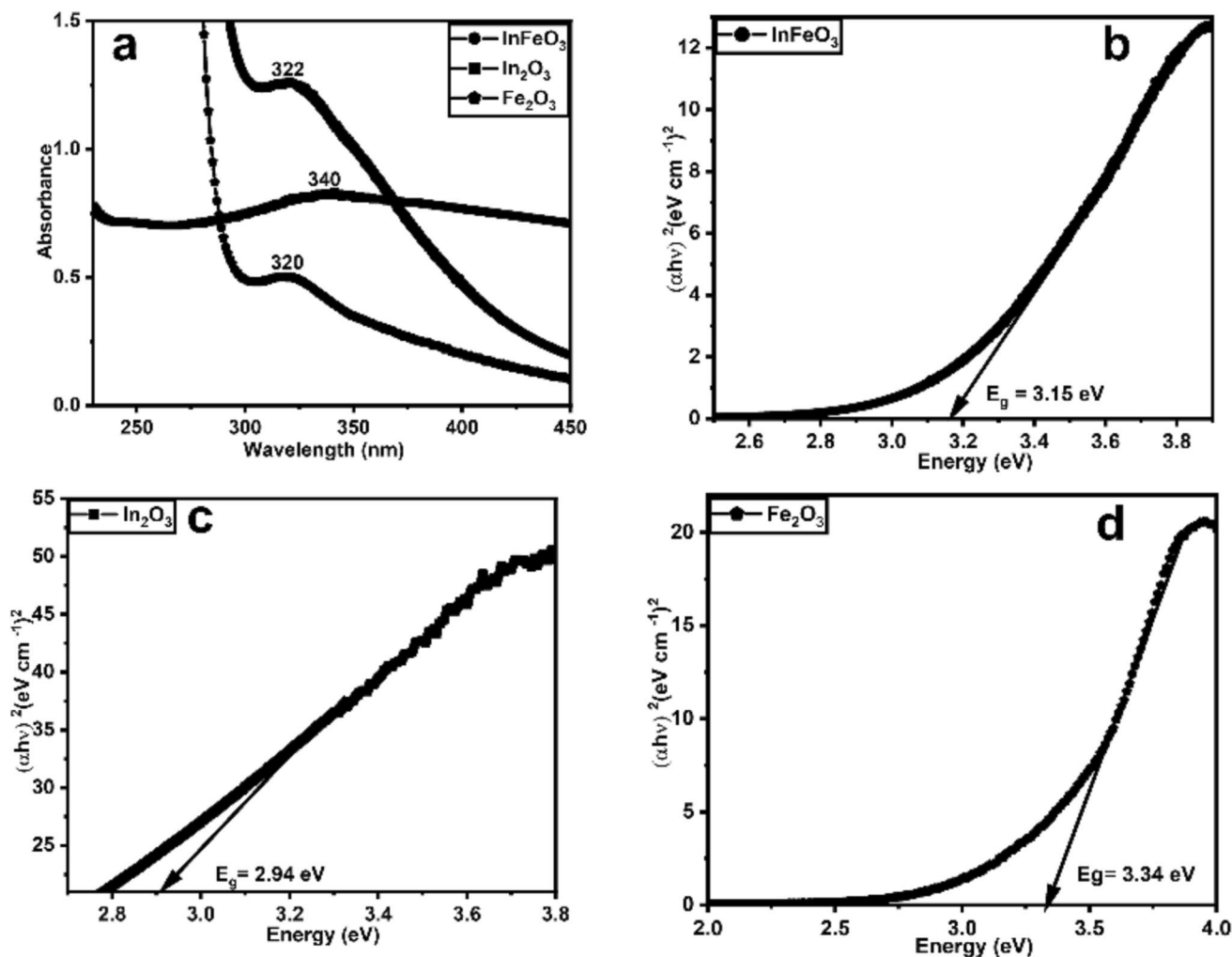


**Fig. 7** a UV–Vis spectra of  $\text{In}_2\text{O}_3$ ,  $\text{Fe}_2\text{O}_3$ , and  $\text{InFeO}_3$  and Tauc plots of **b**  $\text{In}_2\text{O}_3$ , **c**  $\text{Fe}_2\text{O}_3$  and **d**  $\text{InFeO}_3$  annealed at  $800^\circ\text{C}$

spectra of the composite [51]. The appearance of the single band at 322 nm for the composite, confirmed the contribution of both metals (In & Fe) in the formation of the InFeO<sub>3</sub> composite. The optical band gaps of the NPs were determined using Tauc Eq. 3

$$\alpha h\nu^n = A(h\nu - E_g) \quad (3)$$

where  $h$  is Planck's constant,  $\nu$  is frequency,  $A$  is a constant,  $E_g$  is the band gap and  $n=2$  for direct band gap [52]. The optical band gap was determined by extrapolating the plot of  $\alpha h\nu^2$  vs  $h\nu$  to x-axis equal to zero. Figure 7b, c and d shows the energy band gap energy values of 2.9, 3.3, and 3.15 eV which are associated with In<sub>2</sub>O<sub>3</sub>, Fe<sub>2</sub>O<sub>3</sub> and InFeO<sub>3</sub>, respectively. The incorporation of two materials to form a composite increases absorption, leading to a reduction in the energy band gap due to charge transfer transitions and therefore an increase in optical conductivity [25, 53]. This red shift may be referred to the sp-d exchange between the band electrons of In<sub>2</sub>O<sub>3</sub> and localized d-electrons related to the doped Fe ions. The p-d and s-d exchange interactions cause to a positive and a negative correction to the valence band and the conduction band edges, namely the conduction band and valence band is lowered or raised, resulting in the small decrease or increase of the optical band gap [54]. The reduction in the bandgap energy of the composite is more conducive to the transition of electrons when exposed to visible light, leading to an enhanced catalysis performance. This reduction in energy band gap can be attributed to the mobile electrons contained in the nanoparticles, and new excitation energy levels created below the regular band gap due to charge transfer from the nanoparticles [55]. This could also suggest that nanoparticles can increase conductivity, and hence the possibility of using the nanocomposites in electrochemical devices and sensing platforms can be explored.

### 3.7 Photoluminescence of the composite material

The room-temperature photoluminescence (PL) spectra revealing distinct optical emission characteristics for In<sub>2</sub>O<sub>3</sub>, Fe<sub>2</sub>O<sub>3</sub> NPs, and InFeO<sub>3</sub> nanoparticles is presented in Fig. 8. The PL spectrum of In<sub>2</sub>O<sub>3</sub> exhibited dual emission bands: a weak ultraviolet (UV) emission at 338 nm, attributed to near band edge transitions, and a stronger, broad visible emission at 439 nm, associated with defect-related recombination, likely involving oxygen vacancies or indium interstitials. The presence of the two PL emission bands at 338 nm and 439 nm is related to the quantum size effect and agrees with reported research [52]. Fe<sub>2</sub>O<sub>3</sub> displayed a weaker UV emission at 336 nm and a more prominent broad band at 398 nm, attributed to electron–hole recombination, potentially influenced by

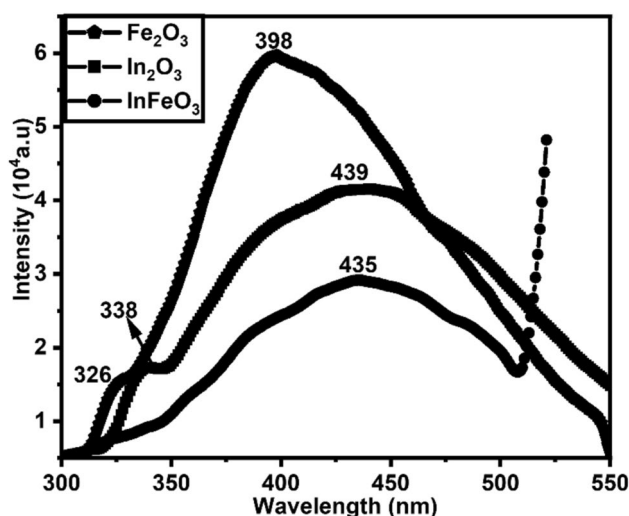
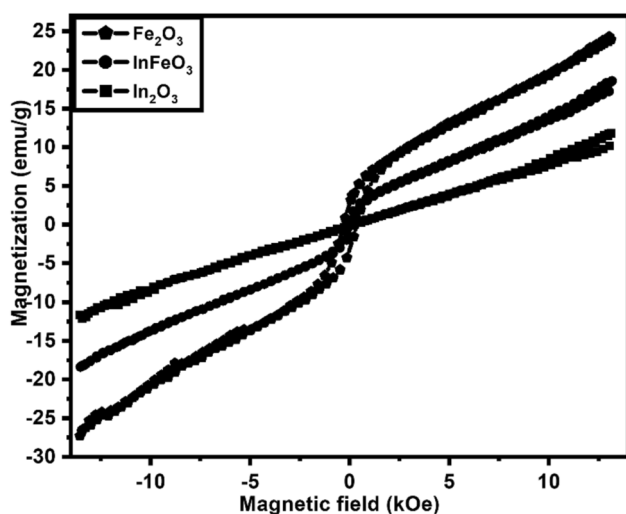


Fig. 8 PL spectra of In<sub>2</sub>O<sub>3</sub>, Fe<sub>2</sub>O<sub>3</sub> and InFeO<sub>3</sub> annealed at 800 °C

excitonic or defect states [56]. The exciton state of Fe<sub>2</sub>O<sub>3</sub> arises from excitation between the valence band, consisting of a mixture of Fe (3d) and O (2p) states, and the conduction band derived primarily from Fe (4s) states. Under excitation of 348 nm irradiation, an electron was excited from the valence band to the conduction band, leaving a hole (+) in the valence band. The InFeO<sub>3</sub> nanocomposite spectrum was dominated by a single broad emission peak at 435 nm, exhibiting a slight blue shift from the In<sub>2</sub>O<sub>3</sub> visible emission and suppression of the UV emission features observed in the individual oxides, suggesting a modification of the electronic environment upon composite formation [56]. Only one emission band can be observed for InFeO<sub>3</sub>, with an excitation of 362 nm. The broad emission peak can be observed to be leaning more toward the In<sub>2</sub>O<sub>3</sub> matrix. However, there was a blue shift from 439 to 435 nm. This blue shift may have originated due to the transition from the interstitial indium level to the valence band and/or the transition from the bottom of the conduction band to the interstitial oxygen level [57]. The corresponding energy band gaps were calculated from the maximum wavelength as 2.82 eV for In<sub>2</sub>O<sub>3</sub>, 3.12 eV for Fe<sub>2</sub>O<sub>3</sub>, and 2.85 eV for InFeO<sub>3</sub>. The lesser values of the energy band gaps observed for PL can be explained by Stokes's shift, which explains the difference between the positions of the band maxima of the absorption and emission spectra of the same electronic transition [58, 59].

### 3.8 VSM analysis of the composite

The field (H) dependence of magnetization (M) curves, M vs. H for In<sub>2</sub>O<sub>3</sub>, Fe<sub>2</sub>O<sub>3</sub> and InFeO<sub>3</sub> were measured at room temperature and are presented in Fig. 9. The derived values of magnetic parameters obtained from the hysteresis



**Fig. 9** M-H hysteresis loops of  $\text{In}_2\text{O}_3$ ,  $\text{Fe}_2\text{O}_3$ , and  $\text{InFeO}_3$  annealed at  $800^\circ\text{C}$

**Table 2** Values of  $H_c$ ,  $M_s$ , and  $M_r$  obtained from the M-H hysteresis loops for  $\text{In}_2\text{O}_3$ ,  $\text{Fe}_2\text{O}_3$ , and  $\text{InFeO}_3$

Material	$H_c$ (kOe)	$M_s$ ( $\text{emu g}^{-1}$ )	$M_r$ ( $\text{emu g}^{-1}$ )
$\text{In}_2\text{O}_3$	0.071	11.94	–
$\text{Fe}_2\text{O}_3$	0.34	26.78	2.89
$\text{InFeO}_3$	0.074	18.48	0.64

loops are presented in Table 2 coercivity ( $H_c$ ), remanence ( $M_r$ ), and maximum magnetization ( $M_s$ ).  $\text{In}_2\text{O}_3$  NPs can be observed to exhibit diamagnetic behavior with  $M_r=0$  and a low value of  $M_s=11.9$  and previous studies reported on the same results, neither the nanocrystalline character nor the high oxygen vacancies concentration seem to be sufficient to lead to magnetic ordering in  $\text{In}_2\text{O}_3$  [60–63]. The magnetization for  $\text{Fe}_2\text{O}_3$  increased with the increase in the magnetic field and saturated ( $M_s$ ) at  $26.78 \text{ emu/g}$ , a value greater than the commercial  $\alpha\text{-Fe}_2\text{O}_3$  nanoparticles. This observation can be attributed to the superparamagnetic properties, which were corroborated by the average size (38 nm) of the synthesized  $\text{Fe}_2\text{O}_3$  obtained by XRD. In addition, this magnetization value may be due to the external surface disordered spin under the applied magnetic field, as reported in the literature [64]. A similar kind of superparamagnetism behavior of  $\text{Fe}_2\text{O}_3$  has been reported for the preparation of hematite nanoparticles by Prabhu et al. [65] and Vinayagam [66].  $\text{InFeO}_3$  exhibited a  $M_s$  value of  $18.48 \text{ emu/g}$  and  $M_r$  of  $0.64 \text{ emu/g}$ . The magnetic ordering can be explained by different mechanisms in the  $\text{In}_2\text{O}_3$  and  $\text{Fe}_2\text{O}_3$  systems. Krishna et al. [67] reported the observed ferromagnetism at room temperature whereby the exchange interaction occurs between dopant cations ( $\text{Fe}^{3+}$ ) through oxygen vacancies

in the  $\text{In}_2\text{O}_3$  matrix. Coey et al. [68] first reported the oxygen vacancies based on ferromagnetic exchange interaction which also correlated to bound magnetic polarons. The magnetization curve was found to be sigmoidal for the  $\text{InFeO}_3$  composite with a decrease in coercivity from  $0.34$  to  $0.007 \text{ kOe}$  and resembled a characteristic of superparamagnetic material [69]. The saturation magnetization  $M_s$  was measured as  $18.480 \text{ emu/g}$ . The decrease in saturation magnetization of the as can be explained by the presence of a non-magnetic material (In) on the surface which may have led to the weakening of exchange interactions in the magnetic core and hence lowered energy of magnetization [70]. The of  $H_c$  value indicated the soft nature of  $\text{InFeO}_3$  composite suggesting that these synthesized ferrites might be useful for the fabrication of switching, sensors, and many other electronic devices.

### 3.8.1 Mössbauer spectroscopy of the composite material

To probe the local atomic environment and magnetic ordering of the iron sites,  $^{57}\text{Fe}$  Mössbauer spectroscopy was performed at room temperature (Fig. 10), showing evidence of the successful incorporation of indium into the iron oxide lattice. The reference spectrum for the pure  $\text{Fe}_2\text{O}_3$  sample displays a well-defined magnetic sextet characteristic of crystalline hematite ( $\alpha\text{-Fe}_2\text{O}_3$ ) with a large hyperfine magnetic field (HMF) indicative of strong Fe–O–Fe superexchange interactions [71]. Conversely, the spectrum for the  $\text{InFeO}_3$  nanocomposite reveals a significant transformation, accurately fitted with two distinct components: a magnetically split sextet with broadened lines and a central paramagnetic quadrupole doublet. The broadening and reduction of the HMF in the sextet, as shown in Table 3, is direct evidence of the substitution of non-magnetic  $\text{In}^{3+}$  ions into the  $\text{Fe}^{3+}$  sites, causing a disruption to the magnetic superexchange pathways and weakening the overall magnetic order [72]. To emphasize this, there is the emergence of the central doublet, representing a sub-population of  $\text{Fe}^{3+}$  ions that are in a paramagnetic state due to being surrounded by a high number of non-magnetic  $\text{In}^{3+}$  ions. This feature, characterized by a quadrupole splitting ( $\Delta$ ) of  $0.384 \text{ mm s}^{-1}$ , confirms the coexistence of  $\text{Fe}^{3+}$  and  $\text{In}^{3+}$  within the  $\text{InFeO}_3$  composite structure [71, 73]. The coexistence of a magnetically weakened sextet and a distinct paramagnetic doublet provides conclusive, atomic-level proof that a true  $\text{InFeO}_3$  nanocomposite was formed, rather than a simple physical mixture of separate  $\text{In}_2\text{O}_3$  and  $\text{Fe}_2\text{O}_3$  phases. The VSM analysis confirms this by a significant reduction in saturation magnetization for  $\text{InFeO}_3$  ( $18 \text{ emu g}^{-1}$ ) compared to pure  $\text{Fe}_2\text{O}_3$  ( $25 \text{ emu g}^{-1}$ ). Ultimately, this strategic integration of tunable magnetism validates the nanocomposite's ability and establishes it as a superior material for developing sensors.

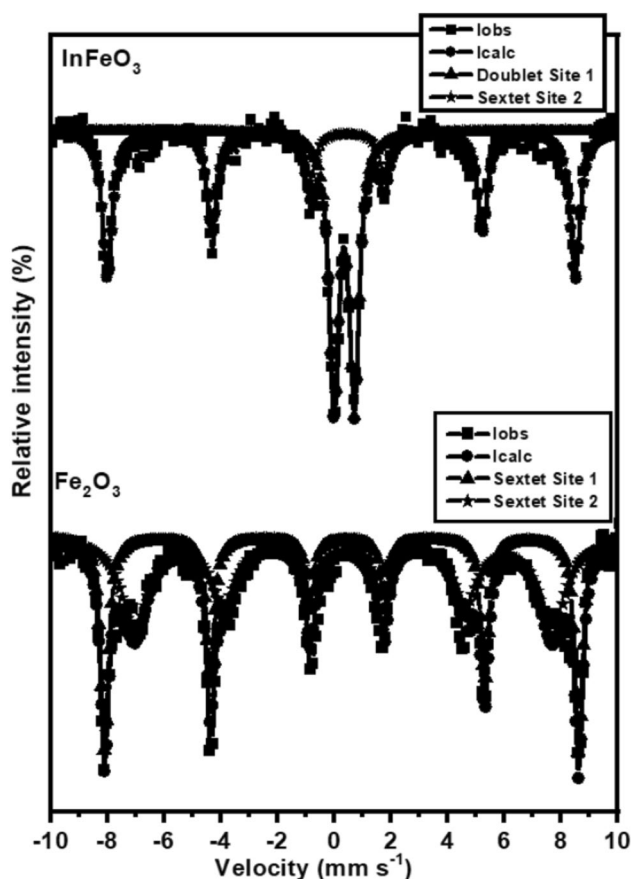


**Fig. 10**  $^{57}\text{Fe}$  Mössbauer spectra room temperature of  $\text{Fe}_2\text{O}_3$  and  $\text{InFeO}_3$

**Table 3** Isomer shifts ( $\delta$ ), hyperfine magnetic fields (H), line widths, quadrupole splitting  $\Delta$  (LW) and fraction population (f) of  $\text{Fe}_2\text{O}_3$  and  $\text{InFeO}_3$

Material	H (kOe)	$\Delta$ (mm $\text{s}^{-1}$ )	$\Delta$ (mm $\text{s}^{-1}$ )	LW (mm $\text{s}^{-1}$ )	f (%)
$\text{Fe}_2\text{O}_3$					
Sextet 1	518	0.372	0.072	0.166	40.6
Sextet 2	456	0.345	0.08	0.538	59.4
$\text{InFeO}_3$					
Sextet 1	511	0.359	0.107	0.197	54.7
Doublet 1	–	0.364	0.72	0.214	45.3

## 4 Electrochemical properties of the composite material

### 4.1 Cyclic voltammetry studies

Cyclic voltammograms for GCE/ $\text{In}_2\text{O}_3$ , GCE/ $\text{Fe}_2\text{O}_3$ , and GCE/ $\text{InFeO}_3$  electrodes in 0.1 M PBS (pH 7.4) at  $50 \text{ mVs}^{-1}$  are presented in Fig. 11. Figure 11a, shows an overlay of all

the modified electrodes for comparison purposes. As seen in Fig. 11a,  $\text{InFeO}_3$  produced the highest current responses compared to the individual materials. GCE/ $\text{In}_2\text{O}_3$ , showed enhanced current compared to the GCE, exhibiting two anodic peaks at 0.01 V and 0.05 V, potentially due to irreversible  $\text{In}_2\text{O}_3$  oxidation or surface hydroxide processes, and a cathodic peak at  $-0.54$  V, indicating a complex reduction process. Figure 11b, GCE/ $\text{Fe}_2\text{O}_3$ , displayed a more defined redox couple attributed to  $\text{Fe}^{3+}/\text{Fe}^{2+}$ , with an anodic peak at  $-0.11$  V, a cathodic peak at  $-0.44$  V, an  $I_{\text{pa}}/I_{\text{pc}}$  ratio of 1.2, and a peak separation ( $\Delta E_p$ ) of 0.58 V, suggesting kinetic limitations. Notably, Fig. 11c, presenting GCE/ $\text{InFeO}_3$ , exhibited the most pronounced response with oxidation and reduction peaks at 0.01 V and  $-0.45$  V respectively, and significantly higher peak currents compared to GCE/ $\text{In}_2\text{O}_3$  and GCE/ $\text{Fe}_2\text{O}_3$ . Figure 11d provides a comparative overlay of the electrochemical responses of  $\text{In}_2\text{O}_3$ ,  $\text{Fe}_2\text{O}_3$ , and  $\text{InFeO}_3$ , highlighting that the oxidation potential region for  $\text{InFeO}_3$  was like  $\text{In}_2\text{O}_3$  but shifted from  $\text{Fe}_2\text{O}_3$ , indicating contributions from both components within the nanocomposite. This enhanced current in GCE/ $\text{InFeO}_3$  suggests a synergistic improvement in electrochemical activity. Therefore, GCE/ $\text{InFeO}_3$  will be the preferred electrode for further studies.

### 4.2 Diffusion coefficient and linear plot studies

The electrochemical performance of the modified electrodes was investigated using Cyclic Voltammetry (CV) to understand the electroactivity properties of the synthesized nanomaterials. Figure 12 displays the CVs for glassy carbon electrode modified with  $\text{In}_2\text{O}_3$  (a),  $\text{Fe}_2\text{O}_3$  (c), and  $\text{InFeO}_3$  (e) recorded at scan rates from 10 to  $100 \text{ mVs}^{-1}$ . This scan rate range was strategically chosen to be fast enough to generate well-defined peaks for these quasi-reversible systems, providing clear insight into their kinetic and diffusion behavior, while avoiding the dominance of capacitive background currents often seen at very high scan rates [74]. While the process is diffusion-controlled, the kinetics of electron transfer were assessed by analyzing the peak potentials. With increasing scan rate, the anodic peaks ( $E_{\text{pa}}$ ) shift to more positive potentials and the cathodic peaks ( $E_{\text{pc}}$ ) shift to more negative potentials. The peak-to-peak separation ( $\Delta E_p$ ) was 0.32 V for  $\text{InFeO}_3$  at a representative scan rate  $50 \text{ mVs}^{-1}$  a significantly larger value than the theoretical  $59/n \text{ mV}$  for an ideal Nernstian system. This behavior is characteristic of a quasi-reversible system, indicating that the rate of electron transfer is finite and not instantaneous [75].

The redox peaks for the individual oxides are attributed to the  $\text{In}^{3+}/\text{In}^+$  ( $\text{In}^{3+} + 2e^- \leftrightarrow \text{In}^+$ ) and  $\text{Fe}^{3+}/\text{Fe}^{2+}$  ( $\text{Fe}^{3+} + e^- \leftrightarrow \text{Fe}^{2+}$ ), respectively [76, 77]. Notably, the  $\text{InFeO}_3$  nanocomposite (Fig. 11e) exhibits a further enhanced current response compared to the individual components as shown in Table 4. A proportional increase in peak current

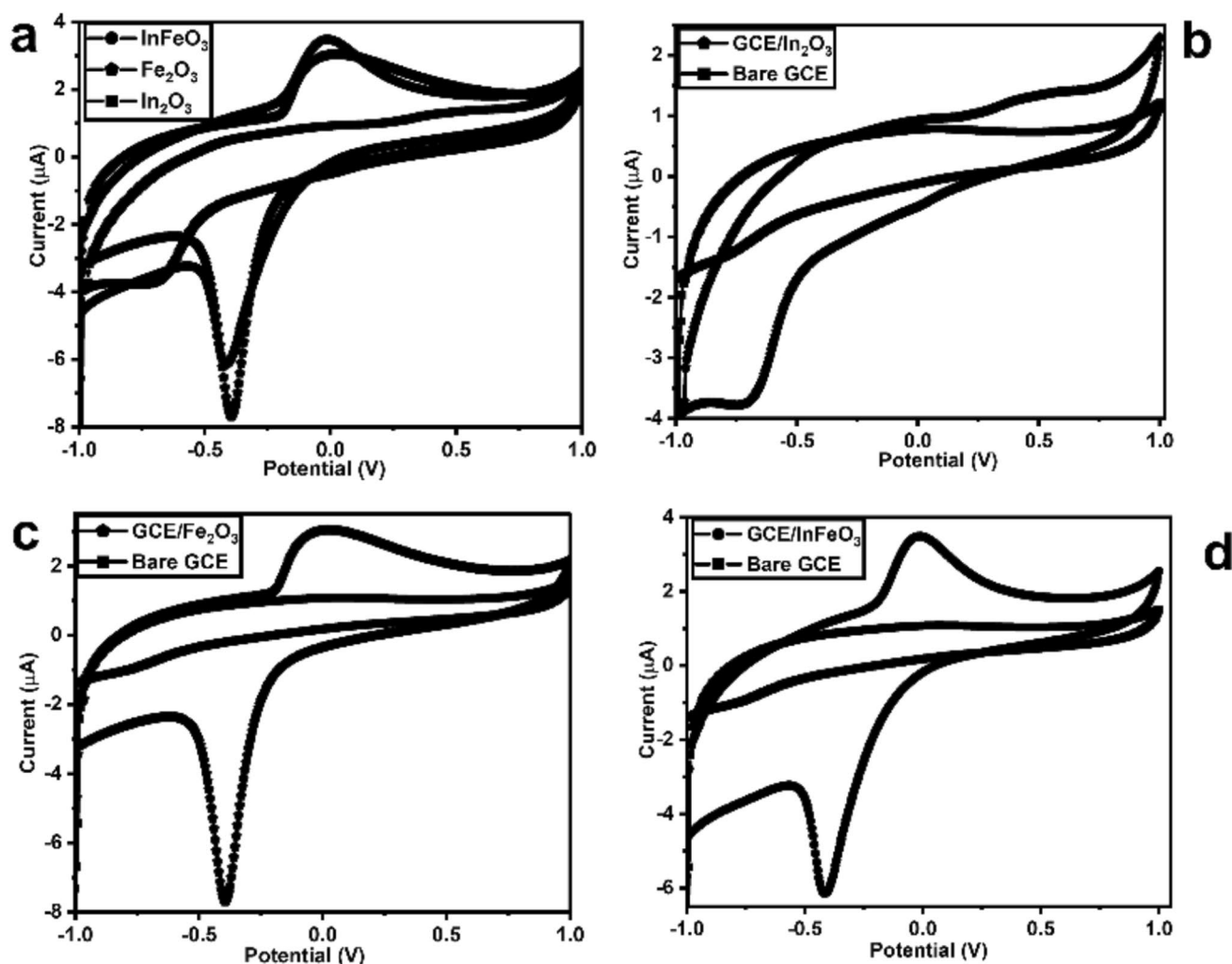


Fig. 11 Cyclic voltammograms of  $\text{In}_2\text{O}_3$ ,  $\text{Fe}_2\text{O}_3$ , and  $\text{InFeO}_3$  @  $50 \text{ mVs}^{-1}$  in 0.1 M PBS, pH 7.4 as a supporting electrolyte

with increase in scan rate was observed, highlighting a synergistic effect that promotes superior electrochemical activity and is shown in Fig. 11b, d, and f. To quantify this enhancement, the diffusion coefficient ( $D$ ) and electroactive surface concentration ( $\Gamma^*$ ) were calculated using the Randles–Ševčík (4) and Brown—Anson (4) equations, respectively [78, 79].

$$I_p = 2.69 \times 105n^{(3/2)}AD^{1/2}Cv^{1/2} \quad (4)$$

and

$$IP/v = (n^2F^2A\Gamma^*)/(4RT) \quad (5)$$

The  $\text{InFeO}_3$ -modified electrode yielded a substantially higher diffusion coefficient and a greater surface concentration compared to the pure  $\text{In}_2\text{O}_3$  and  $\text{Fe}_2\text{O}_3$ , confirming that the  $\text{InFeO}_3$  nanocomposite provides a more conductive and reactive interface, facilitating more efficient

charge and mass transport. The combined results establish the green-synthesized  $\text{InFeO}_3$  nanocomposite as a superior material for electrochemical applications.

## 5 Conclusion

Green synthesis of  $\text{In}_2\text{O}_3$ ,  $\text{Fe}_2\text{O}_3$  and  $\text{InFeO}_3$  was successfully achieved by using coffee extract as a reducing agent. The optical band gap of the NPs was found to be within 2.19–3.3 eV range for which was confirmed by UV–Vis and PL. The difference in the band gap of the composite that of  $\text{In}_2\text{O}_3$  and  $\text{Fe}_2\text{O}_3$  NPs indicated the existence of strong quantum confinement. HRSEM measurements revealed that most of the nanoparticles are quasi-spherical grains agglomerated together. The nanoparticles' spherical morphology was observed because of the annealing process. This morphology of the nanoparticles agreed with

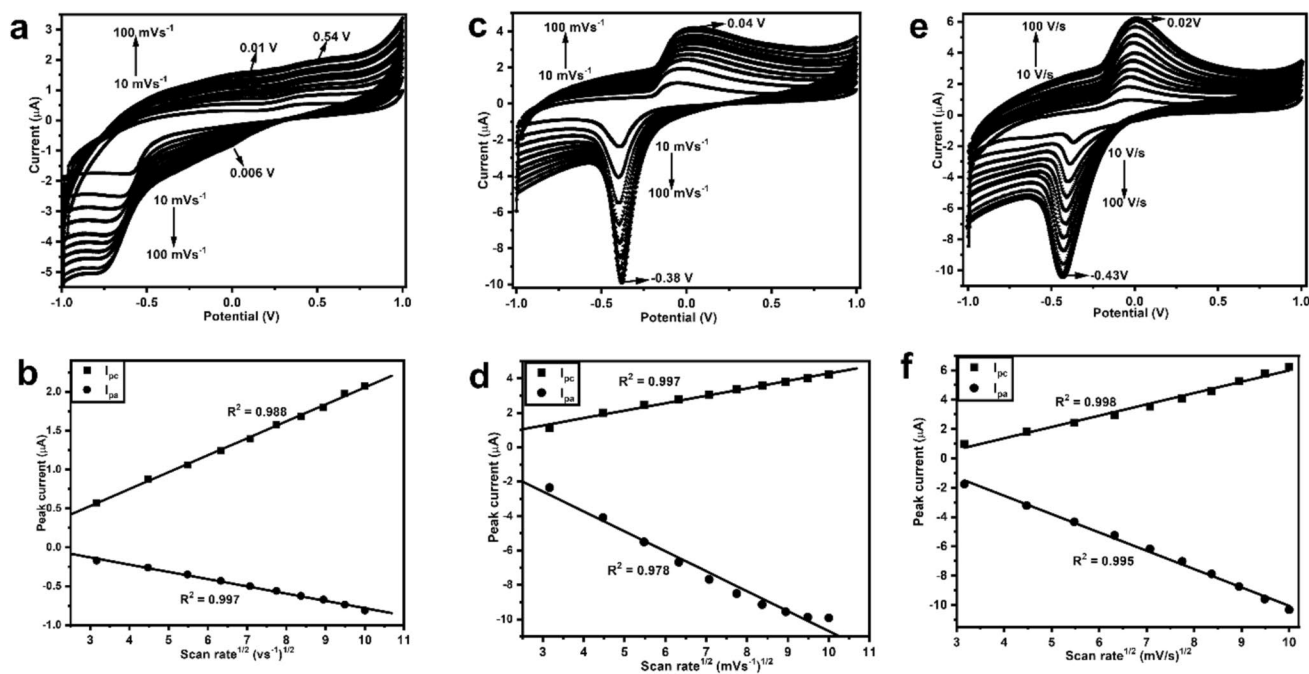


**Fig. 12** Cyclic voltammograms for  $\text{In}_2\text{O}_3$ ,  $\text{Fe}_2\text{O}_3$ , and  $\text{InFeO}_3$  at different scan rates from 10 to  $100 \text{ mVs}^{-1}$  (a, c, and e), and the corresponding linear plots (b, d, and f)

**Table 4** Summary of the calculated parameters from CV

Nanoparticle	Diffusion coefficient ( $\text{cm}^2 \text{ s}^{-1}$ )	Surface concentration ( $\text{mol cm}^{-2}$ )
$\text{In}_2\text{O}_3$	$5.23 \times 10^{-6}$	$1.28 \times 10^{-8}$
$\text{Fe}_2\text{O}_3$	$8.45 \times 10^{-5}$	$3.25 \times 10^{-7}$
$\text{InFeO}_3$	$9.72 \times 10^{-5}$	$4.62 \times 10^{-7}$

the images obtained from TEM. EDX showed the presence of both In and Fe and O elements in the  $\text{InFeO}_3$  elemental analysis, confirming the formation of the composite. FTIR confirmed the existence of the In–O, and Fe–O vibrational bonds in the synthesized composite. The XRD measurements confirmed a pure and crystalline phase for  $\text{In}_2\text{O}_3$ ,  $\text{Fe}_2\text{O}_3$  and  $\text{InFeO}_3$ . This observation agreed with the SAED images obtained from the HRTEM measurements. From the Scherer equation, the average particle size was estimated from XRD data to be 34, 38, and 27.3 nm for  $\text{In}_2\text{O}_3$ ,  $\text{Fe}_2\text{O}_3$ , and  $\text{InFeO}_3$ , respectively. The particle size deduced from HRTEM was 31.9, 36.7, and 34.8 nm and the particle size estimated from SAXS was 27.6, 24, and 27 nm  $\text{In}_2\text{O}_3$ ,  $\text{Fe}_2\text{O}_3$ , and  $\text{InFeO}_3$ , respectively. The particle size seemed to vary from each instrument but was in close agreement. The electrochemical properties of  $\text{InFeO}_3$  were successfully studied. The results revealed quasi-reversibility for a

one-electron transfer reaction. The nature of the reaction taking place at the electrode surface was confirmed to be a diffusion-controlled process. The electrochemical parameters examined revealed that the composite can be a good candidate for the sensor application.

**Author contributions** NPN and UF wrote the initial main manuscript. ZT, JJ, TM, RFNA and EI revised the manuscript. All authors reviewed the manuscript.

**Funding** Open access funding provided by University of South Africa. This study was funded by the National Research Foundation (NRF), South Africa. We would also like to acknowledge CHIETA for additional funding.

**Data availability** No datasets were generated or analysed during the current study.

## Declarations

**Competing interests** The authors declare no competing interests.

**Open Access** This article is licensed under a Creative Commons Attribution 4.0 International License, which permits use, sharing, adaptation, distribution and reproduction in any medium or format, as long as you give appropriate credit to the original author(s) and the source, provide a link to the Creative Commons licence, and indicate if changes were made. The images or other third party material in this article are included in the article's Creative Commons licence, unless indicated otherwise in a credit line to the material. If material is not included in the article's Creative Commons licence and your intended use is not

permitted by statutory regulation or exceeds the permitted use, you will need to obtain permission directly from the copyright holder. To view a copy of this licence, visit <http://creativecommons.org/licenses/by/4.0/>.

## References

- Hossain N, Rimon MIH, Mimona MA, Mobarak MH, Ghosh J, Islam MA, Al Mahmud MZ (2024) Prospects and challenges of sensor materials: a comprehensive review. *e-Prime-Adv Electr Eng Electron Energy* 7:100496
- Jalalvand AR, Karami MM (2025) Roles of nanotechnology in electrochemical sensors for medical diagnostic purposes: a review. *Sens Bio-Sens Res* 47:100733
- Shashanka R, Adimule V (2022) Optical and sensor characteristics of nanocomposites. Scientific Books Collection
- Huang XY, Chi ZT, Liu J, Li DH, Sun XJ, Yan C et al (2020) Enhanced gas sensing performance based on p-NiS/n-In<sub>2</sub>O<sub>3</sub> heterojunction nanocomposites. *Sensors Actuat B: Chem* 304:12305
- Pourmadadi M, Ahmadi MJ, Dinani HS, Ajalli N, Dorkoosh F (2022) Theranostic applications of stimulus-responsive systems based on Fe<sub>2</sub>O<sub>3</sub>. *Pharm Nanotechnol* 10(2):90–112
- Neri G, Bonavita A, Galvagno S, Siciliano P, Capone S (2022) CO and NO<sub>2</sub> sensing properties of doped-Fe<sub>2</sub>O<sub>3</sub> thin films prepared by LPD. *Sens Actuat B: Chem* 82(1):40–47
- Fazio E, Spadaro S, Corsaro C, Neri G, Leonardi SG, Neri F et al (2021) Metal-oxide based nanomaterials: synthesis, characterization and their applications in electrical and electrochemical sensors. *Sensors* 21(7):2494
- Bulowski W, Knura R, Socha RP, Basiura M, Skibińska K, Wojnicki M (2024) Thin film semiconductor metal oxide oxygen sensors: limitations, challenges, and future progress. *Electronics* 13(17):3409
- Huston M, DeBella M, DiBella M, Gupta A (2021) Green synthesis of nanomaterials. *Nanomaterials* 11(8):2130
- Kobylińska N, Klymchuk D, Khaynakova O, Duplij V, Matvieieva N (2022) Morphology-controlled green synthesis of magnetic nanoparticles using extracts of ‘hairy’ roots: environmental application and toxicity evaluation. *Nanomaterials* 12(23):4231
- Pechyen C, Tangnorawich B, Toommee S, Marks R, Parcharoen Y (2024) Green synthesis of metal nanoparticles, characterization, and biosensing applications. *Sens Int* 5:100287
- Yadav G, Mathur J (2024) Seed priming with fruit and vegetable waste-based nanoparticles: a sustainable green approach. *J Soil Sci Plant Nutr* 25:1–19
- Ahmed SF, Mofijur M, Rafa N, Chowdhury AT, Chowdhury S, Nahrin M et al (2022) Green approaches in synthesising nanomaterials for environmental nanobioremediation: technological advancements, applications, benefits and challenges. *Environ Res* 204:111967
- Alangari A, Alqahtani MS, Shahid M, Syed R, Goel M, Lakshminpathy R, Kaur K (2024) Green synthesis of FeO nanoparticles from coffee and its application for antibacterial, antifungal, and anti-oxidation activity. *Green Process Synth* 13(1):20230268
- Gebre L, Welderfael T, Desta MB (2023) Optimization of reaction conditions for green synthesis of silver nanoparticles using *Coffea arabica* leave extract. *Methods* 33:35
- Shah S, Hussain S, Din STU, Shahid A, Amu-Darko JNO, Wang M et al (2024) A review on In<sub>2</sub>O<sub>3</sub> nanostructures for gas sensing applications. *J Environ Chem Eng* 12:112538
- Begi AN, Hussain S, Liaqat MJ, Alsaiari NS, Ouladsmane M, Qiao G, Liu G (2024) Unlocking low-concentration NH<sub>3</sub> gas sensing: an innovative MOF-derived In<sub>2</sub>O<sub>3</sub>/Co<sub>3</sub>O<sub>4</sub> nanocomposite approach. *Mater Sci Semicond Process* 181:108641
- Rajyashree L, Manoharan C, Loganathan A, Venkateshwarlu M (2023) Electrochemical and sensing properties of  $\alpha$ -Fe<sub>2</sub>O<sub>3</sub> nanoparticles synthesized using hydrothermal method at low reaction temperature. *J Mater Sci: Mater Electron* 34(6):462
- Salkar, K. Y. (2020). *Study of structural, electrical, magnetic and optical properties of dilute magnetic semiconductor nanoparticles* (Doctoral dissertation, Goa University)
- Kumar DV, Bansal DMK (2024) Investigating magnetic, optical, and structural properties of Mn & Fe doped In<sub>2</sub>O<sub>3</sub> nanoparticles. <https://doi.org/10.2139/ssrn.4510262>
- Dhamodaran M, Karuppannan R, Murugan R, Boukhvalov DW, Pandian MS, Perumalsamy R (2022) Morphology controlled synthesis of Fe and Mn co-doped In<sub>2</sub>O<sub>3</sub> nanocubes and their Dopant-Atom effects on electronic structure and magnetic properties. *J Magn Magn Mater* 560:169547
- Oliveira AA, Valerio-Cuadros MI, De Brito AS, Tupan LFS, Barco R, Ivashita FF, Paesano A Jr (2022) Magnetic behavior and site occupancy in Fe-doped In<sub>2</sub>O<sub>3</sub> nanoparticles. *J Magn Magn Mater* 547:168944
- Zhang Y, Qin C, Zhang R, Zhang Y, Wang Y, Zhang Z, Cao J (2022) Construction of hierarchical In<sub>2</sub>O<sub>3</sub>/In<sub>2</sub>S<sub>3</sub> microsphere heterostructures for TEA detection. *J Materiomics* 8(6):1113–1121
- Prerna DI, Govindaraju K, Tamilselvan S, Kannan M, Vasantharaja R, Chaturvedi S, Shkolnik D (2021) Influence of nanoscale micro-nutrient  $\alpha$ -Fe<sub>2</sub>O<sub>3</sub> on seed germination, seedling growth, translocation, physiological effects and yield of rice (*Oryza sativa*) and maize (*Zea mays*). *Plant Physiol Biochem* 162:564–580
- Cani D, Cuyvers T, Pescarmona PP (2025) Indium-iron oxide nanosized solid solutions as photocatalysts for the degradation of pollutants under visible radiation. *Chemsuschem* 18(3):e202401180
- Zhang B, Seki M, Zhou H, Chen J, Tabata H (2020) InFeO<sub>3</sub> photoelectrode with two-dimensional superlattice for visible-and ultraviolet-light-driven water splitting. *APL Mater* 8(5):051107
- Revathi S, Srimathi R, Kumar A, Kaur J, Yuvaraj S, Ubaidullah M et al (2024) Monitoring the effect of In<sup>3+</sup> doping on the structural, morphological, optical, vibrational, and magnetic properties of perovskite LaFeO<sub>3</sub> nanoparticles. *Inorg Chem Commun* 168:112777
- Bierwagen O (2015) Indium oxide—a transparent, wide-band gap semiconductor for (opto) electronic applications. *Semicond Sci Technol* 30(2):024001
- Bora, D. K., Braun, A., Erat, S., Safonova, O., Graule, T., & Constable, E. C. (2011). Evolution of structural properties of iron oxide nano particles during temperature treatment from 250°C–900°C: X-ray diffraction and Fe K-shell pre-edge X-ray absorption study. *arXiv preprint arXiv:1111.6204*.
- Erichsen SCV, Assenmacher W, Schnakenburg G, Mader W (2014) Synthesis and crystal structure of InFeO<sub>3</sub>(ZnO)<sub>4</sub>. *Z Anorg Allg Chem* 640(14):2817–2822
- Dong Z, Hu W, Ma Z, Li C, Liu Y (2019) The synthesis of composite powder precursors via chemical processes for the sintering of oxide dispersion-strengthened alloys. *Mater Chem Front* 3(10):1952–1972
- Bashir AKH, Mayedwa N, Kaviyarasu K, Razanamahandry LC, Matinise N, Bharuth-Ram K et al (2019) Investigation of electrochemical performance of the biosynthesized  $\alpha$ -Fe<sub>2</sub>O<sub>3</sub> nanorods. *Surfaces Interfaces* 17:100345
- Aslibeiki B, Kameli P, Salamati H, Eshraghi M, Tahmasebi T (2010) Superspin glass state in MnFe<sub>2</sub>O<sub>3</sub> nanoparticles. *J Magn Magn Mater* 322(19):2929–2934
- Sangale SS, Jadhav VV, Shaikh SF, Shinde PV, Ghule BG, Raut SD et al (2020) Facile one-step hydrothermal synthesis and room-temperature NO<sub>2</sub> sensing application of  $\alpha$ -Fe<sub>2</sub>O<sub>3</sub> sensor. *Mater Chem Phys* 246:122799

35. Zhang C, Pei Y, Zhao LD, Berardan D, Dragoe N, Gong S, Guo H (2014) The phase stability and thermophysical properties of  $\text{InFeO}_3$  ( $\text{ZnO}$ )  $m$  ( $m = 2, 3, 4, 5$ ). *J Eur Ceram Soc* 34(1):63–68
36. Caminade AM, Turrin CO, Laurent R, Ouali A, Delavaux-Nicot B (eds) (2011) *Dendrimers: towards catalytic, material, and biomedical uses*. John Wiley & Sons
37. Goertz V, Dingenouts N, Nirschl H (2009) Comparison of nanometric particle size distributions as determined by SAXS, TEM and analytical ultracentrifuge. *Part Part Syst Charact* 26(1–2):17–24
38. Will R, Rein C, Frank J, Malan J (2025) High heterogeneity in the size distribution of the micellar fraction from in vitro digestions: sample preparation and reporting recommendations. *J Sci Food Agric* 105:3406–3415
39. Mourdikoudis S, Pallares RM, Thanh NT (2018) Characterization techniques for nanoparticles: comparison and complementarity upon studying nanoparticle properties. *Nanoscale* 10(27):12871–12934
40. Kumar S (2006) Spectroscopy of organic compounds. *Cosmic Rays* 10:4
41. Rasheed RT, Al-Algawi SD, Tariq SZ (2014) Preparation and study of indium oxide nanoparticles. *Iraqi J Appl Phys* 10:4
42. Ullah H, Yamani ZH, Qurashi A, Iqbal J, Safeen K (2020) Study of the optical and gas sensing properties of  $\text{In}_2\text{O}_3$  nanoparticles synthesized by rapid sonochemical method. *J Mater Sci: Mater Electron* 31(20):17474–17481
43. Goh KW, Johan MR, Wong YH (2018) Enhanced structural properties of  $\text{In}_2\text{O}_3$  nanoparticles at lower calcination temperature synthesised by co-precipitation method. *Micro Nano Letters* 13(2):270–275
44. Azam S (2017) Preparation and properties of thermo and magneto responsive superabsorbent nanocomposite hydrogel. *Mater Lett* 89:12–15
45. Navada KM, Nagaraja GK, D'Souza JN, Kouser S, Ravikumar CR, Manasa DJ (2021) Bio-fabrication of multifunctional quasi-spherical green  $\alpha\text{-Fe}_2\text{O}_3$  nanostructures for paracetamol sensing and biomedical applications. *Ceram Int* 47(23):33651–33666
46. Boyatzis SC, Velivasaki G, Malea E (2016) A study of the deterioration of aged parchment marked with laboratory iron gall inks using FTIR-ATR spectroscopy and micro hot table. *Heritage Sci* 4(1):1–17
47. Krehula S, Ristić M, Reissner M, Kubuki S, Musić S (2017) Synthesis and properties of indium-doped hematite. *J Alloy Compd* 695:1900–1907
48. Huang LM, Araújo CM, Ahuja R (2009) Magnetic and electronic properties of 3d transition-metal-doped  $\text{In}_2\text{O}_3$ : an ab initio study. *Europhys Lett* 87(2):27013
49. Tien LC, Hsieh YY (2014) Defect-induced ferromagnetism in undoped  $\text{In}_2\text{O}_3$  nanowires. *Mater Res Bull* 60:690–694
50. Khan H, Swati IK (2016)  $\text{Fe}^{3+}$ -doped anatase  $\text{TiO}_2$  with d-d transition, oxygen vacancies and  $\text{Ti}^{3+}$  centers: synthesis, characterization, UV-vis photocatalytic and mechanistic studies. *Ind Eng Chem Res* 55(23):6619–6633.
51. Zhang GY, Xu YY, Gao DZ, Sun YQ (2011)  $\alpha\text{-Fe}_2\text{O}_3$  nanoplates: PEG-600 assisted hydrothermal synthesis and formation mechanism. *J Alloy Compd* 509(3):885–890
52. Pavithra N, Nirmala M, Priyadharshini S, Kavitha U, Kavitha B (2024) Influence of pH on structural, optical and magnetic properties of undoped and Ni-doped  $\alpha\text{-Fe}_2\text{O}_3$  nanoparticles for antimicrobial activity. *Nano-Structures & Nano-Objects*, 37:101098.
53. Souza JS, Alves LL, Lima AF (2022) Effects of tensile strain on the electronic, optical and ferroelectric properties of a multifunctional R3c  $\text{InFeO}_3$  compound. *Comput Mater Sci* 215:111788
54. Ahmed TY, Aziz SB, Dannoun EM (2024) New photocatalytic materials based on alumina with reduced band gap: a DFT approach to study the band structure and optical properties. *Heliyon* 10:5
55. Khan A, Rahman F, Ahad A, Alvi PA (2020) Investigation of transport phenomenon and magnetic behavior of Fe doped  $\text{In}_2\text{O}_3$ . *Physica B* 592:412282
56. Moore MC (2013) *Metal oxide nanostructured materials for optical and energy applications*. University of California, Berkeley
57. Lassoued A, Lassoued MS, Dkhil B, Ammar S, Gadri A (2018) Synthesis, photoluminescence and magnetic properties of iron oxide ( $\alpha\text{-Fe}_2\text{O}_3$ ) nanoparticles through precipitation or hydrothermal methods. *Physica E* 101:212–219
58. Sun X, Ma K, Li W (2018) Formation of Fe-doped  $\text{In}_2\text{O}_3$  nanowires and influence evolution of Fe ions on its photoluminescence property. *J Alloy Compd* 764:861–868
59. Liu X, Xu Z, Cole JM (2013) Molecular design of UV-vis absorption and emission properties in organic fluorophores: toward larger bathochromic shifts, enhanced molar extinction coefficients, and greater Stokes shifts. *J Phys Chem C* 117(32):16584–16595
60. Raevskaya AE, Ivanchenko MV, Stroyuk OL, Kuchmiy SY, Plyusnin VF (2015) Luminescent Ag-doped  $\text{In}_2\text{S}_3$  nanoparticles stabilized by mercaptoacetate in water and glycerol. *J Nanopart Res* 17:1–12
61. Chandradass J, Bae DS, Kim KH (2011) A simple method to prepare indium oxide nanoparticles: structural, microstructural and magnetic properties. *Adv Powder Technol* 22(3):370–374
62. Bérardan D, Guilmeau E, Pelloquin D (2008) Intrinsic magnetic properties of  $\text{In}_2\text{O}_3$  and transition metal-doped- $\text{In}_2\text{O}_3$ . *J Magn Magn Mater* 320(6):983–989
63. Karade VC, Parit SB, Dawkar VV, Devan RS, Choudhary RJ, Kedge VV, Chougale AD (2019) A green approach for the synthesis of  $\alpha\text{-Fe}_2\text{O}_3$  nanoparticles from *Gardenia resinifera* plant and its in vitro hyperthermia application. *Heliyon* 5(7):e02044
64. Miri A, Khatami M, Sarani M (2020) Biosynthesis, magnetic and cytotoxic studies of hematite nanoparticles. *J Inorg Organomet Polym Mater* 30(3):767–774
65. Prabhu P, Rao M, Murugesan G, Narasimhan MK, Varadavenkatesan T, Vinayagam R et al (2022) Synthesis, characterization and anticancer activity of the green-synthesized hematite nanoparticles. *Environ Res* 214:113864
66. Vinayagam R, Pai S, Varadavenkatesan T, Narasimhan MK, Narayanasamy S, Selvaraj R (2020) Structural characterization of green synthesized  $\alpha\text{-Fe}_2\text{O}_3$  nanoparticles using the leaf extract of *Spondias dulcis*. *Surf Interf* 20:100618
67. Krishna NS, Kaleemulla S, Amarendra G, Rao NM, Krishnamoorthi C, Kuppam M, Omkaram I (2015) Structural, optical, and magnetic properties of Fe doped  $\text{In}_2\text{O}_3$  powders. *Mater Res Bull* 61:486–491
68. Coey JMD, Venkatesan M, Fitzgerald CB (2005) Donor impurity band exchange in dilute ferromagnetic oxides. *Nat Mater* 4(2):173–179
69. Rath K, Sen S (2019) Garlic extract based preparation of size controlled superparamagnetic hematite nanoparticles and their cytotoxic applications. *Indian J Biotechnol* 18:108–118
70. Peddis D, Yaacoub N, Ferretti M, Martinelli A, Piccaluga G, Musino A, Fiorani D (2011) Cationic distribution and spin canting in  $\text{CoFe}_2\text{O}_4$  nanoparticles. *J Phys: Condens Matter* 23(42):426004
71. Downie LJ, Goff RJ, Kockelmann W, Forder SD, Parker JE, Morrison FD, Lightfoot P (2012) Structural, magnetic and electrical properties of the hexagonal ferrites  $\text{MFeO}_3$  ( $M = \text{Y}, \text{Yb}, \text{In}$ ). *J Solid State Chem* 190:52–60
72. Nodari I, Alebouyeh A, Brice JF, Gerardin R, Evrard O (1988) Caractérisation de nouveaux ferrites d'indium:  $\text{In}_2\text{Fe}_4\text{O}_9$  et  $\text{InFeO}_3$ . *Mater Res Bull* 23(7):1039–1044
73. Prakasam BA, Lahtinen M, Peuronen A, Manikandan G, Muruganandham M, Sillanpää M (2018) Synthesis of self-assembled

- mesoporous 3D  $\text{In}_2\text{O}_3$  hierarchical micro flowers composed of nanosheets and their electrochemical properties. *RSC Adv* 8(45):25856–25865
74. Jjagwe J, Olupot PW, Kulabako R, Carrara S (2024) Electrochemical sensors modified with iron oxide nanoparticles/nanocomposites for voltammetric detection of Pb (II) in water: a review. *Helvion*. 10:e29743
  75. Zhang K, Hou D, Wu D, Li Y, He X, Sun T et al (2025) A nonenzymatic electrochemical sensor for highly sensitive detection of thiophanate methyl based on MWCNTs functionalized bimetallic Fe/Cu MOF. *J Food Compos Anal* 139:107144
  76. Dong Y, Ghuman KK, Popescu R, Duchesne PN, Zhou W, Loh JY et al (2018) Tailoring surface frustrated Lewis pairs of  $\text{In}_2\text{O}_{3-x}(\text{OH})_y$  for gas-phase heterogeneous photocatalytic reduction of  $\text{CO}_2$  by isomorphous substitution of  $\text{In}^{3+}$  with  $\text{Bi}^{3+}$ . *Adv Sci* 5(6):1700732
  77. Rafeeq M, Ahmad S, Sami A, Khan KZ, Haidar Z, Ahmed F et al (2025) Facile hydrothermal fabrication of  $\text{In}_2\text{O}_3/\text{Fe}_2\text{O}_3$  as a potential electrode material for supercapacitor. *Electrochimica Acta* 524:145963
  78. Adarakatti PS (2025) Fundamentals of electrochemistry. *Agricultural electrochemistry*. American Chemical Society, pp 17–46
  79. Madagalam M (2025) Enhancing the Electron Transfer at Electrochemical Interfaces by Spinel Oxide-Nanostructures.

**Publisher's Note** Springer Nature remains neutral with regard to jurisdictional claims in published maps and institutional affiliations.

## Authors and Affiliations

Nokwanda Precious Ngema<sup>1</sup> · Usisipho Feleni<sup>2</sup> · Ziyanda Tshobeni<sup>1</sup> · Jaymi January<sup>1</sup> · Takalani Mulaudzi<sup>3</sup> · Emmanuel Iwuoha<sup>1</sup> · Rachel Fanelwa Ngece-Ajayi<sup>1</sup>

✉ Usisipho Feleni  
felenu@unisa.ac.za

✉ Rachel Fanelwa Ngece-Ajayi  
fngece@uwc.ac.za

<sup>1</sup> SensorLab (University of the Western Cape Sensor Laboratories), University of the Western Cape, 4th Floor Chemical Sciences Building, Robert Sobukwe Road, Bellville, Cape Town 7535, South Africa

<sup>2</sup> Institute for Nanotechnology and Water Sustainability (iNanoWS), College of Science, Engineering and Technology, University of South Africa, Florida Campus, Florida Park 1710, Johannesburg, South Africa

<sup>3</sup> Department of Biotechnology, University of the Western Cape, Bellville, South Africa